Failure of Autophagy–Lysosomal Pathways in Rod Photoreceptors Causes the Early Retinal Degeneration Phenotype Observed in *Cln6*[nclf] Mice

Philipp von Eisenhart-Rothe,[1] Alexandra Grubman,[2] Ursula Greferath,[1] Linda J. Fothergill,[1] Andrew I. Jobling,[1] Joanna A. Phipps,[1] Anthony R. White,[2] Erica L. Fletcher,[1] and Kirstan A. Vessey[1]

[1]Department of Anatomy and Neuroscience, The University of Melbourne, Melbourne, Victoria, Australia
[2]Department of Pathology, The University of Melbourne, Melbourne, Victoria, Australia

Purpose. Vision loss caused by photoreceptor death represents one of the first symptoms in neuronal ceroid lipofuscinosis, a condition characterized by accumulation of intracellular waste. *Cln6*[nclf] mice have a naturally occurring mutation in ceroid–lipofuscinosis neuronal (CLN) protein 6 and are a model of this disorder. In order to identify the effect intracellular waste (lipofuscin) accumulation plays in driving retinal degeneration, the time course of degeneration was carefully characterized functionally using the electroretinogram and structurally using histology.

Methods. *Cln6*[nclf] and C57BL/6J, wild-type, mice were studied at postnatal day 18 (P18), P30, P60, P120, and P240, and retinal degeneration was correlated with changes in the retinal pigment epithelial (RPE) and neuronal autophagy–lysosomal pathways using super-resolution microscopy.

Results. In *Cln6*[nclf] mice there was significant loss of rod photoreceptor function at P18, prior to photoreceptor nuclei loss at P60. In contrast, cone pathway function was not affected until P240. The loss of rod photoreceptor function correlated with significant disruption of the autophagy–lysosomal degradation pathways within photoreceptors, but not in the RPE or other retinal neurons. Additionally, there was cytosolic accumulation of P62 and undigested mitochondrial-derived, ATP synthase subunit C in the photoreceptor layers of *Cln6*[nclf] mice at P30.

Conclusions. These results suggest that rod photoreceptors have an increased sensitivity to disturbances in the autophagy–lysosomal pathway and the subsequent failure of mitochondrial turnover, relative to other retinal cells. It is likely that primary failure of the rod photoreceptors rather than the RPE or other retinal neurons underlies the early visual dysfunction that occurs in the *Cln6*[nclf] mouse model.

Keywords: retina, photoreceptor, rodent, autophagy, lysosome, ceroid-lipofuscinosis neuronal protein 6, CLN6, neuronal ceroid lipofuscinosis, NCL, neurodegeneration, super-resolution microscopy, electroretinogram

Neuronal ceroid lipofuscinoses (NCLs) are a group of inherited lysosomal storage disorders that lead to progressive neurodegeneration and are characterized by early vision loss, late-stage motor dysfunction, and premature death.[1,2] The pathomorphologic hallmark of all NCLs is the accumulation of intracellular waste in the form of autofluorescent lipofuscin and ceroid lipopigments in nonmitotic cell types such as neurons.[1,2] With a worldwide incidence of 1 in 100,000, mutations in a range of genes encoding ceroid lipofuscinosis neuronal proteins (*CLN* in humans; *Cln* in mice) cause various forms of the disease based on the age of onset and severity of disease progression (infantile, late infantile, juvenile, and adult).[3,4] In particular, mutations in the *CLN6* gene result in a late infantile variant form of NCL due to dysfunctional CLN6 protein. CLN6 has been suggested to play a significant role in the intracellular recycling process of the autophagy–lysosome pathway, modulating the regulation of lysosomal pH and lysosome-associated

proteins.[5–7] Despite this, the CLN6 protein does not directly colocalize with lysosome markers and is instead expressed at the endoplasmic reticulum where its function is currently unknown.[5–7] Thus, the molecular mechanism of lysosomal failure that leads to severe neurodegeneration in patients with *CLN6* mutations remains unclear.

The naturally occurring *Cln6*[nclf] mouse, which has a single nucleotide insertion in exon 4 of the *Cln6* gene that induces a frameshift and a premature stop codon, provides a valuable tool for assessing the role of CLN6 in the neurodegenerative process.[8,9] Studies of the ocular phenotype in the *Cln6*[nclf] mouse model reveal an early and progressive loss of photoreceptor cells in the outer nuclear layer (ONL), with relative preservation of the inner retina.[10,11] Retinal function declines from 1 month of age, stemming from a decrease in rod photoreceptor function; however, the effect on the cone pathway function has not been assessed.[10,11] Histologic

investigation and work at the ultrastructural level show cytoplasmic inclusions and lysosomal accumulations in many different retinal cell types.[10] In addition, activation of the local immune response (amoeboid microglia) and Müller cell gliosis are apparent.[11] Despite this work, the mechanisms that lead to lipofuscin accumulation, early photoreceptor death, and ultimately vision loss in the *Cln6^{nclf}* mouse are unknown.

Intracellular accumulation of lipofuscin in the retinal pigment epithelium (RPE) has long been suspected to play a major role in a range of retinal degenerations, including age-related macular degeneration (AMD)[12] and Stargardt's disease.[13] Failure of the autophagy–lysosomal pathway and accumulation of lipofuscin has been found to cause significant impairment in the RPE, resulting in photoreceptor dysfunction and subsequent vision loss in these diseases.[14,15] This is also the case for other *Cln* mutants.[16,17] Alternatively, lysosomal accumulations within the photoreceptors themselves may induce photoreceptor failure and retinal degeneration as has been suggested in the fly.[18] As *Cln6^{nclf}* mice are characterized by deposits of lipofuscin in retinal neurons and the RPE, they provide a useful model for identifying which cell type is predominantly responsible for retinal degeneration. In the present study, the function of the autophagy–lysosomal pathway was investigated in RPE, photoreceptors, and inner retinal neurons in the *Cln6^{nclf}* mouse model to determine whether failure of the RPE or a primary photoreceptor dysfunction induces retinal degeneration. To investigate this, the time course of retinal degeneration was carefully characterized in *Cln6^{nclf}* mice with age and correlated with changes in the autophagy–lysosomal pathways in the RPE and retinal neurons using super-resolution microscopy. The results provide novel insights into the mechanism of lipofuscin accumulation in the retinal neurons and RPE as well as its effect on photoreceptor function and survival in *Cln6^{nclf}* mice.

METHODS

Animals

Cln6^{nclf} on a C57BL/6J background were obtained from the Jackson Laboratory (Stock No: 003605; Bar Harbour, ME, USA) and annually backcrossed to C57BL/6J mice obtained from the Animal Resources Centre (Canning Vale, WA, Australia). C57BL/6J (wild-type, WT) control mice were obtained from the Animal Resources Centre. Animals were housed at the University of Melbourne animal facility, under a 12:12-hour light:dark cycle with ad libitum access to food and water. Genotyping of the *Cln6^{nclf}* mice was performed as specified previously.[19] All experiments and handling of animals were conducted in compliance with the standards of the ARVO Statement for the Use of Animals in Ophthalmic and Vision Research as well as the institutional guidelines of The University of Melbourne Animal Ethics Committee (AEC) (Ethics ID 1513553). Experiments were completed on animals aged to postnatal day 18 (P18), P30, P60, P120, and P240.

Fundus Imaging

In vivo imaging was used to investigate ocular fundus appearance in WT and *Cln6^{nclf}* retinae at P30 to P240 using a Micron III Retinal Imaging Microscope (Phoenix Technology Group, Pleasanton, CA, USA). As previously described,[20,21] light-adapted animals ($n = 6$) were deeply anesthetized by an intraperitoneal injection of a mixture of ketamine (67 mg/kg; Provet, Heatherton, VIC, Australia) and xylazine (13 mg/kg; Troy Laboratories, Glendenning, NSW, Australia). The corneal reflex was suppressed by applying 0.5% proparacaine hydro-

chloride (Alcaine; Alcon Laboratories, Frenchs Forest, NSW, Australia), while dilation of the pupils was facilitated by the topical application of 1% atropine sulfate (Alcon Laboratories) and 2.5% phenylephrine hydrochloride (Bausch&Lomb, Chatswood, NSW, Australia). Mice were positioned in a custom-made holder, the lens of the Micron III microscope was applied close to the cornea, and the fundus of each mouse was viewed and images were captured using the Micron III software (Phoenix Technology Group).

Electroretinography to Assess Rod and Cone Pathway Function

Retinal function of the rod and cone pathway of WT and *Cln6^{nclf}* mice was assessed at P18 ($n = 7$–10), P30 ($n = 10$), P60 ($n = 8$), P120 ($n = 9$–10), and P240 ($n = 8$–9) using a twin-flash electroretinogram (ERG). Animals were dark adapted overnight, deeply anesthetized, and the corneal reflex/dilation altered as above. Full-field responses were captured using custom-made Ag/AgCl electrodes, a custom-made Ganzfeld, and a commercial flash unit (Nikon SB900, Rhodes, NSW, Australia). Two 2.1 log cd.s/m² full-field flashes were separated by an 0.8-second interstimulus interval (ISI), to evoke mixed rod and cone (Flash 1, F1) and subsequent cone ERG responses (F2).[22–24] The responses were amplified (gain ×5000; −3 decibel [dB] at 1 Hz and 1 kHz, ML132 BioAmp; ADInstruments, Bella Vista, NSW, Australia) and acquired at a 10-kHz sampling frequency over a 250-ms period (ML785 Powerlab/8sp amplifier; ADInstruments). Provision of the stimulus and recording of the ERG were coordinated by Scope software version 3.6.10 (ADInstruments).

For the analysis of ERG, the rod pathway response was generated by digital subtraction of the cone ERG from the mixed ERG signal.[23,24] The rod pathway responses were modeled and waveform components representing the rod photoreceptor a-wave (PIII), postphotoreceptor b-wave (PII), and oscillatory potentials (OPs, summed amplitudes of OPs 2–4) were assessed as previously described.[23,25] OP1 and OP5 of the rod OPs were not included as they are often small and difficult to distinguish from system noise and so we included only OPs 2, 3, and 4 in our analysis as they could be consistently measured. Cone pathway responses were modeled and waveform components for the postphotoreceptor responses, the cone b-wave (PII), and OPs (summed OPs 1, 2, and 3) were assessed as previously described.[23,25] Differences in genotype and age were analyzed in GraphPad Prism v7 (GraphPad, La Jolla, CA, USA) for each rod and cone pathway ERG component using a 2-way ANOVA, including a Tukey multiple comparisons test, with $P < 0.05$ considered significant.

Electroretinography to Assess Rod Photoreceptor Recovery Kinetics

The kinetics of rod photoreceptor recovery was assessed in P30, dark-adapted WT and *Cln6^{nclf}* mice ($n = 11$) using a modification of the twin-flash (F1, F2) protocol above. To assess changes in rod photoreceptor recovery rate, twin-flash ERG responses were recorded as described above and ISIs between F1 and F2 were varied between 0.8 and 4, 8, 16, 32, 64, 128, and 180 seconds, while intervals between F2 and F1 of the next recording were kept at 180 seconds. The F2/F1 ratios of photoreceptor a-wave amplitudes were calculated for each ISI, averaged, and plotted and the kinetics of photoreceptor recovery was analyzed using nonlinear regression (hyperbolic equation) in GraphPad Prism. Differences in genotype and ISI were analyzed using a 2-way ANOVA including a Tukey

TABLE 1. Primary Antibodies for Immunohistochemical Analysis

Target	Antibody/Lectin	Dilution	Source	Immunogen
Amacrine and ganglion cells	Mouse anti-calretinin, monoclonal	1:500	Catalog No. 63B; Swant, Bellinzona, Switzerland	Recombinant human calretinin-22k
Müller cells	Mouse anti-glutamine synthetase, GS, monoclonal, GS-6	1:1000	Catalog No. MAB302; Millipore, Merck, Bayswater, VIC, Australia	Glutamine synthetase purified from sheep brain
Cones	Fluorescein-labeled peanut agglutinin, PNA, from Arachis hypogaea (peanuts)	1:200	Catalog No. FL-1071; Vector Laboratories, Burlingame, CA, USA	NA
Mitochondria	Mouse anti-MTCO1, monoclonal	1:5000	Catalog No. AB14705; Abcam, Melbourne, VIC, Australia Sapphire Bioscience, NSW, Australia	Purified mitochondrial Complex IV subunit I, human
Autophagosomes	Rabbit anti-microtubule associated protein light chain 3 isoform B, LC3B, polyclonal	1:300	Catalog No. NB100-2220; Novus Biologicals, Littleton, CO, USA	Synthetic peptide to N-terminal portion of the human LC3 protein sequence
Lysosomes	Rat anti-lysosomal associated membrane protein 1, LAMP1, monoclonal	1:50	Catalog No. 1D4B, Developmental Studies Hybridoma Bank, Iowa City, IA, USA	NIH/3T3 mouse embryo fibroblast tissue culture cell membranes
Mitochondria and protein aggregation	Rabbit anti-ATP synthase C, monoclonal	1:100	Catalog No. AB181243; Abcam, Sapphire Bioscience, NSW, Australia	Synthetic peptide within Human ATP synthase C aa 50 to the C-terminus
Autophagic degradation/ protein aggregation	Mouse anti-p62/SQSTM1, monoclonal	1:200	Catalog No. H00008878-M01; Novus Biologicals, Littleton, CO, USA	SQSTM1 full-length recombinant protein with GST tag

multiple comparisons test, with $P < 0.05$ considered significant.

Histology for Analysis of Retinal Layer Thickness

Retinal morphology and layer thickness were assessed in WT and *Cln6^{nclf}* mice at P18, P30, P60, P120, and P240 ($n \geq 5$ each group) using toluidine blue–stained resin sections as previously described.[26] Mice were deeply anesthetized (as above) and killed by cervical dislocation. The eyes were enucleated and the posterior eye cups were fixed overnight in 1% paraformaldehyde, 2.5% glutaraldehyde, 3% sucrose, and 0.01% calcium chloride in 0.1 M phosphate buffer, pH 7.4 (PB). Following fixation, eye cups were washed in PB and subsequently dehydrated in a series of methanol solutions (75%, 85%, 95%, and 100%) and a final acetone (100%) step. Dehydrated tissues were then incubated in a mixture of Epon resin (ProSciTech, Thuringowa Central, QLD, Australia), embedded, and polymerized at 60°C overnight. Eye orientation was not accounted for. Semithin sections (1-µm thickness) of the eye cups were collected using an ultramicrotome (Reichert-Jung Ultracut S; Reichert, Depew, NY, USA) and stained with 1% toluidine blue. Sections were washed, mounted with resin, and sealed with a glass coverslip.

To determine the thickness of each retinal layer, brightfield images of central retinal resin sections were captured using a ×20 air objective and Tile Scan mode on a confocal laser scanning microscope (LSM 510 META; Carl Zeiss AG, Jena, Germany). Retinal layers were analyzed for one half of the retinal section, covering the area from optic nerve to the tip of the periphery, and then partitioned into the three sections, central, midperiphery, and periphery, based on the length of the covered area. Using a custom segmentation script for ImageJ v1.47 (National Institutes of Health, Bethesda, MD, USA), the thickness (µm) of the ganglion cell layer (GCL), inner plexiform layer (IPL), inner nuclear layer (INL), ONL, inner and outer photoreceptor segments (IS/OS),

and total retina was obtained. Differences in genotype and age for each layer, were analyzed using a 2-way ANOVA including a Tukey multiple comparisons post test (GraphPad Prism, $P < 0.05$).

Immunohistochemistry and Super-Resolution Confocal Microscopy

Fluorescence immunohistochemistry as well as detection of autofluorescence was used to investigate various retinal cell types, cellular organelles, aggregated protein structures, and accumulated lipofuscin in the retinae of WT and *Cln6^{nclf}* mice at P18, P30, P60, P120, and P240 ($n \geq 5$ each group). For tissue collection and analysis of autophagy–lysosomal pathways, P30 animals were euthanized at the same time of the day (12 PM to 1 PM), to detect maximum levels of autophagy.[27] After dissection, posterior eye cups were fixed for 30 minutes in 4% paraformaldehyde dissolved in PB, washed three times in PB, and incubated in a series of graded concentrations of sucrose (10%, 20%, 30% vol/vol in PB) for cryoprotection. For sectioning, the eye cups were embedded in OCT cryopreservation medium (Tissue-Tek O.C.T, Sakura; Torrance, CA, USA) and frozen. Sections were cut transversely at 14 µm (Leica CM1860 UV, Wetzlar, Germany), placed onto poly-L-lysine–coated slides (Menzel-Gläser, Braunschweig, Germany), and stored at −30°C until further use. For labeling, slides were defrosted, washed three times in PB, and incubated overnight with either a single antibody or a combination of primary antibodies (Table 1). Primary antibodies were diluted in antibody buffer (3% vol/vol normal goat serum, 1% wt/vol bovine serum albumin, 0.05% wt/vol sodium azide, 0.5% vol/vol Triton X-100 in PB). After incubation, sections were washed in PB and incubated for 90 minutes in a mixture of the nuclear dye 4′,6-diamidino-2-phenylindole (DAPI; Life Sciences, Scoresby, VIC, Australia) and corresponding Alexa Fluor–conjugated secondary antibodies (Life Sciences) diluted in antibody buffer at 1:300 and 1:500, respectively. Sections were

washed, covered with Dako mounting medium (Agilent Technologies, Santa Clara, CA, USA) and a glass coverslip.

Images were captured by a confocal laser scanning microscope (LSM 800, Carl Zeiss AG), using a ×20 air, ×0 oil, and ×63 oil immersion objective at a resolution of 2048 × 2048 pixels. Excitation lasers included a diode 40-nm laser with emission filter set 445/50; an Argon 488-nm laser with emission filter set 515/565; a DPSS 561-nm laser with emission filter set 615; and a HeNe 633-nm laser with emission filter set 615. After acquisition, all images collected in super resolution, Airyscan mode was deconvolved using the Airyscan processing function (ZEN software, Carl Zeiss AG). For comparison of WT and *Cln6^nclf* tissue sections, all imaging settings were kept at the same levels. After scale bars were digitally added, images were adjusted for brightness, contrast, and black levels in Adobe Photoshop CC (Adobe Systems Incorporated, San Jose, CA, USA), keeping equal settings between WT and *Cln6^nclf* mice for consistency.

Quantification of Müller Cell Number

To determine whether there was a change in Müller cell number, retina from WT and *Cln6^nclf* mice at P240 ($n = 6$) were labeled with glutamine synthetase (GS; Table 1) and entire sections, which included the optic nerve head, imaged using a ×20 air objective and Tile Scan mode on the confocal. To count GS-positive cells, a line was drawn through the center of the IPL and a custom ImageJ-Microsoft Excel (Redmond, WA, USA) macro used to threshold and detect cell processes that crossed the line. Differences between genotype for GS counts were analyzed using a Student's *t*-test (GraphPad Prism, $P < 0.05$).

Quantification of Autophagic Degradation

To assess the autophagy–lysosomal pathway in different retinal layers, WT and *Cln6^nclf* retinae at P30 ($n = 6$) were taken and sections labeled using a combination of LC3B antibody (autophagosomes) and LAMP1 antibody (lysosomes; Table 1). For the individual retinal layers, the RPE, the ONL, and the INL, two super-resolution z-stack images per retina were collected in super resolution, Airyscan mode using a ×63 oil objective. To account for chromatic aberration at the super-resolution level, z-stack images of TetraSpec microspheres (Thermofisher Scientific, Melbourne, VIC, Australia) were captured and used to detect and reject misaligned x, y, and z-stack slices for each image. For the quantification of autophagosome and lysosome number (puncta number/area of region of interest μm^2), average puncta size (μm^2), as well as colocalization of autophagosomes and lysosomes in each retinal layer, images were assessed using a custom script in FIJI (https://fiji.sc/, provided in the public domain by National Institutes of Health). Briefly, regions of interest were created to define the individual retinal layers, and intensity thresholding for each channel was applied. Local maxima were used for the detection and quantification of vesicles in thresholded regions of interest for each channel. Colocalization of vesicles was measured using the area of coincidence. Differences between genotype for autophagosome and lysosome number, average size, and colocalization in each layer were analyzed using a 2-way ANOVA with a Tukey multiple comparisons test (GraphPad Prism, $P < 0.05$).

Western Blot Analysis

To assess for changes in autophagy–lysosomal degradation between WT and *Cln6^nclf* retinae, Western blot analyses for LC3B-I to LC3B-II ratio and P62/SQSTM1 expression levels were completed. WT and *Cln6^nclf* retinae were collected from

$n = 5$ animals at P30. To assess the effect of blocking autophagy–lysosomal degradation, for each animal, one retina was incubated in culture media with 50 µM chloroquine (autophagy–lysosomal blocker; Sigma-Aldrich Corp. (Cat. No. C6628-25G; St. Louis, MO, USA) and the other without, for 24 hours at 37°C in a humidified cell culture chamber with 5% CO_2.[28] The culture media consisted of Alpha minimum essential medium (Hyclone, Cat. No. M4526-500ML; Sigma-Aldrich Corp.), 1% L-glutamine (Gibco, Cat. No. 25030081; ThermoFisher Scientific), 1% penicillin–streptomycin (Cat. No. 15140-148; Gibco), 10% fetal bovine serum (Cat. No. SH30071.03; In Vitro Technologies, Noble Park North, VIC, Australia). Western blot was completed as previously described.[29] Briefly, retinae were placed in 30 µL homogenizing buffer and the cell contents lysed by sonication. Samples were spun at 7000*g* for 1 minute to pellet cell debris and the supernatant used for Western blot analysis. Protein samples (reducing conditions, samples not boiled) of 40 µg/lane were run on a 4% to 12% gradient Acrylamide-Bis Tris gel (Bolt Bis-Tris 4%-12%, 12 well, Cat. No. NW04122BOX; Thermofisher Scientific) along with a molecular weight marker (Chameleon Duo Prestained Protein Ladder; Cat. No. LCR-928-60000, Millenium Science, Mulgrave, VIC, Australia). Proteins were separated by electrophoresis and transferred onto polyvinylidene difluoride (PVDF) membranes (Transfer stack: PVDF iBlot Stack; Cat. No. IB24002; Thermofisher Scientific). After blocking, the LC3B antibody (1:500 dilution) or the P62/SQSTM1 antibody (1:500) was applied, along with an antibody against β-actin as a protein loading control (1:1000, Cat. No. PA121167; Thermofisher Scientific). After incubation in primary antibody overnight, membranes were washed and incubated with the secondary antibodies (IRDye 680LT Goat anti-rabbit IgG, Cat. No. LCR-926-68021; IRDye 800CW Goat anti-rabbit IgG, Cat. No. LCR-926-32211; IRDye 800CW Goat anti-mouse IgG, LCR-925-32210; Millenium Science). After washing, the membranes were imaged using an Odyssey CLx Infrared imaging system (Odyssey-Licor system, Millenium Science) and the same settings used for all blots. Band density was analyzed using ImageJ and normalized to β-actin. LC3B results were expressed as a ratio of LC3B-II to LC3B-I, while P62 results were expressed as arbitrary fluorescence units. Differences between genotype and chloroquine treatment groups were analyzed using a 2-way ANOVA with a Tukey multiple comparisons test (GraphPad Prism, $P < 0.05$).

RESULTS

Cln6^nclf Mice Show Accumulation of White Lesions in the Fundus From Postnatal Day 60

Representative fundus images were taken in vivo from P30, P60, P120, and P240 in *Cln6^nclf* mice and compared to WT controls (Fig. 1). WT mice displayed a healthy fundus up to P240 (8 months of age; Fig. 1A). At P30, the fundus of *Cln6^nclf* mice was similar to that of WT controls, showing normal pigmentation and vascular morphology (Fig. 1B). From P60 onward, *Cln6^nclf* mice showed progressive accumulation of white fundus lesions (Fig. 1C), so that by P240 the entire retinal field displayed signs of discrete ocular lesions (Fig. 1D).

Retinal Function Is Impaired From Postnatal Day 18 in *Cln6^nclf* Mice

Rod pathway responses of dark-adapted WT and *Cln6^nclf* mice were assessed using a twin-flash ERG at P18, P30, P60, P120,
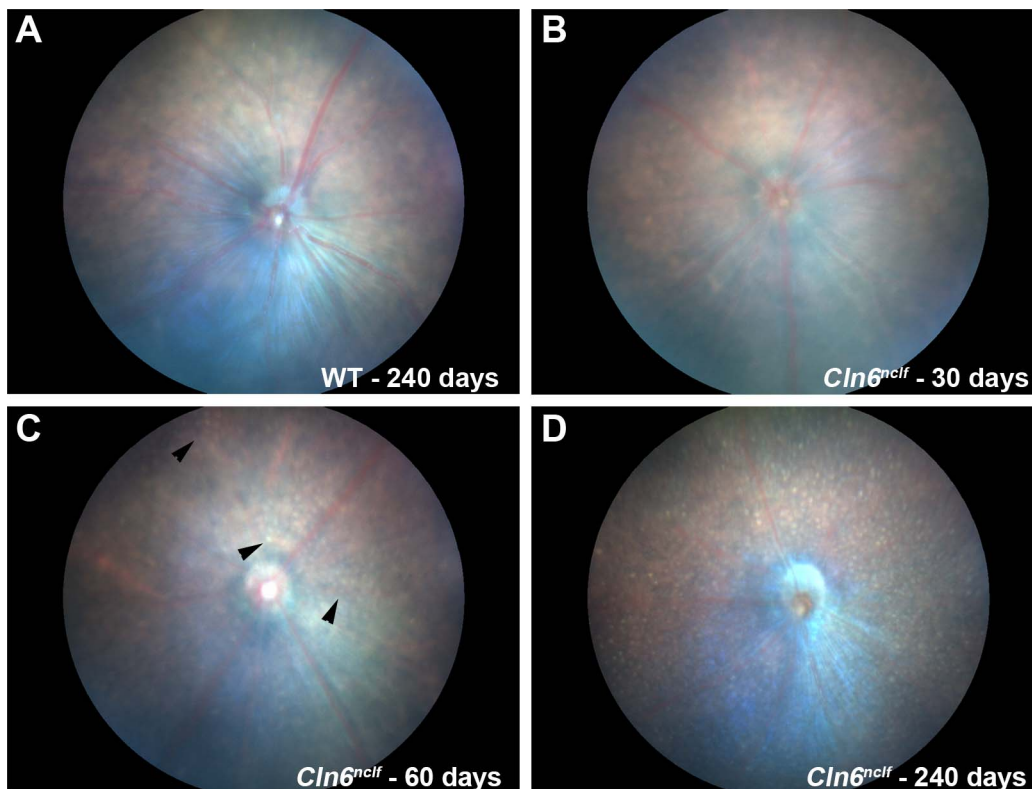
FIGURE 1. *Cln6^{nclf}* mice show accumulation of white lesions in the fundus from postnatal day 60. Ocular fundus images were collected from WT and *Cln6^{nclf}* retinae at P30 through P240 using a Micron III Retinal Imaging camera. (**A**) At P240, WT mice had a healthy fundus appearance including normal pigmentation and blood vessel morphology. (**B**) At P30, the fundus appearance of *Cln6^{nclf}* mice was similar to that of WT controls. (**C**, **D**) From P60, *Cln6^{nclf}* mice displayed discrete white lesions in the ocular fundus (*black arrows*), which increased out to P240.

and P240 (Fig. 2). Representative rod pathway waveforms of WT (black line) and *Cln6^{nclf}* mice (gray line) at P18 through P240 indicate a progressive loss of ERG amplitude from P18 in *Cln6^{nclf}* mice (Fig. 2A). The individual ERG waveform components were modeled and the rod photoreceptor response (a-wave, PIII Rmax) was found to be significantly reduced in *Cln6^{nclf}* mice from P18 (Fig. 2B). By P240 only a small, residual rod photoreceptor response was apparent in *Cln6^{nclf}* mice when compared to the WT controls. Despite this dysfunction, the kinetics of rod photoreceptor recovery was not altered at P30 between *Cln6^{nclf}* (gray circle) and WT mice (black square; Fig. 2C). As was seen for the rod photoreceptor response, the modeled b-wave (PII amplitude) reduced significantly from P18 in *Cln6^{nclf}* mice relative to the WT response (Fig. 2D). To assess if the postphotoreceptor decline in the b-wave (PII) of *Cln6^{nclf}* mice was dependent on or independent from the decline of the photoreceptor response, the percentage loss of the modeled a-wave (PIII, gray circle) and b-wave (PII, gray square) was compared (Fig. 2E). At all ages investigated, the reduction in the postphotoreceptor response (b-wave, PII) was not greater than that which could be attributed to failure of rod photoreceptor function (a-wave, PIII). In contrast, the PII response was sometimes larger than might be expected, indicating that photoreceptor to bipolar cell transmission is not linear and/or there may be inner retinal compensation from P60 to P240. Analysis of the rod OPs showed that neither the individual OP amplitudes nor the summed amplitudes of OP2 to OP4 were significantly different between WT and *Cln6^{nclf}* mice until P120, at which time OPs 2, 3, and 4 were all reduced (summed OPs, Fig. 2F; individual data for OPs not shown).

This suggests a relative sparing of inner retinal function until later stages of degeneration.

Cone pathway function of WT (black) and *Cln6^{nclf}* mice (gray) was investigated using a twin-flash ERG, and representative raw cone ERG waveforms at P18, P120, and P240 are shown (Fig. 3A). There were no changes in cone pathway function observed in *Cln6^{nclf}* mice relative to WT controls until P240, when the cone postphotoreceptor response (b-wave, PII; Fig. 3B) and the summed cone OPs (Fig. 3C) were reduced.

Photoreceptor Layer Thickness Is Reduced From Postnatal Day 60 in *Cln6^{nclf}* Mice, While the Inner Retinal Layers Are Preserved

With rod pathway function reduced from P18 in *Cln6^{nclf}* mice, histologic analysis for retinal layer thickness for WT and *Cln6^{nclf}* mice was undertaken to identify the retinal cell types affected. Retina from WT and *Cln6^{nclf}* mice were fixed and prepared as semithin, toluidine blue–stained resin sections for analysis, and representative images from central retina are presented (Figs. 4A–I). There were no apparent differences in retinal layer thickness between WT and *Cln6^{nclf}* mice at P18 (Figs. 4A, 4B) and P30 (Figs. 4C, 4D); however, from P60 onward there was progressive loss of the photoreceptor layers (ONL) in *Cln6^{nclf}* mice (Figs. 4E, 4F). By P240, *Cln6^{nclf}* mice had between two and three layers of photoreceptor nuclei in central regions (Fig. 4H), while some regions completely lacked photoreceptors in the midperipheral to peripheral eccentricities (Fig. 4I inset in Fig. 4H). Despite this outer retinal cell loss, there was no loss of inner retinal layers apparent in *Cln6^{nclf}* mice at any age investigated (Figs. 4A–I).
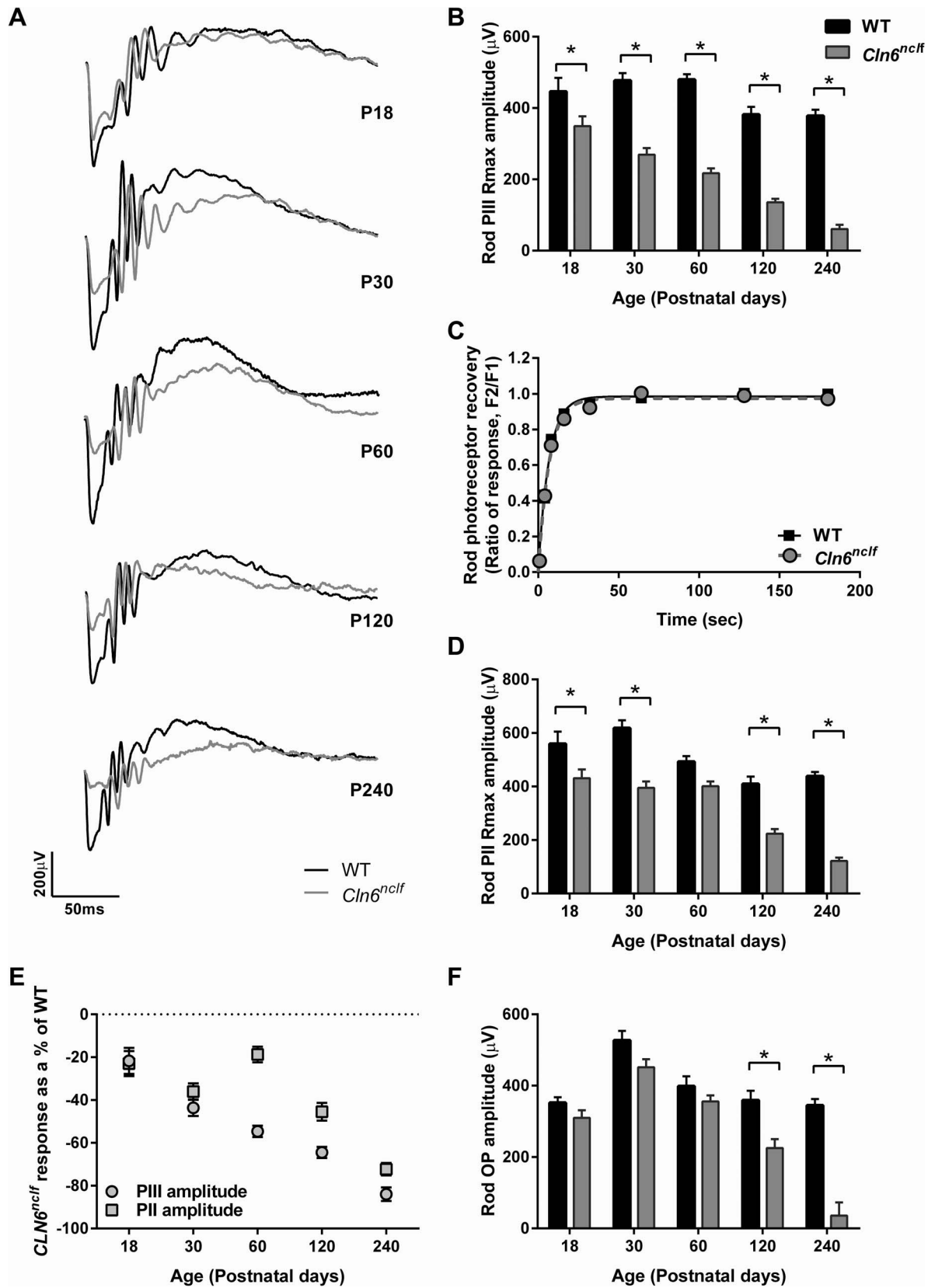
FIGURE 2. Rod photoreceptor dysfunction precedes inner retinal functional losses in *Cln6^nclf* mice. Rod pathway function was assessed in vivo using a twin-flash ERG (flash 2.1 log cd.s/m^2) in WT and *Cln6^nclf* mice at P18 through P240. (**A**) Representative rod pathway ERG waveforms are shown, highlighting loss of ERG amplitude from P18 onward in the *Cln6^nclf* mice (*gray line*) when compared with age-matched WT controls (*black line*). (**B**) Rod photoreceptor function (a-wave, PIII Rmax) is reduced in *Cln6^nclf* mice from P18. (**C**) The time for the rod photoreceptor response to recover between twin flashes from the first (F1) to the second flash (F2) is not altered between WT and *Cln6^nclf* mice at P30. (**D**) Rod postphotoreceptor function (b-wave, PII Rmax) is reduced in *Cln6^nclf* mice from P18. (**E**) Both rod photoreceptor (PIII, *circle*) and

postphotoreceptor (PII, *square*) responses decline with age in *Cln6^nclf* mice, and loss of the postphotoreceptor can be attributed to loss of photoreceptor input. (**F**) Rod postphotoreceptor OP amplitudes (summed amplitudes of OPs 2–4) were reduced in *Cln6^nclf* mice from P120. All data are expressed as mean ± SEM for $n \geq 7$ mice at each age. Data were analyzed by a 2-way ANOVA including a Tukey multiple comparisons test with P values < 0.05 considered significant (*).

Retinal layer thickness was quantified in central, midperipheral, and peripheral regions for WT (black bars) and *Cln6^nclf* mice (gray bars), and the data for central regions are presented in Figures 4J through 4N. Photoreceptor IS/OS progressively declined in thickness in *Cln6^nclf* mice from P120 (Fig. 4J), while ONL thickness significantly reduced from P60 onward (Fig. 4K). In contrast, no significant changes were observed between WT and *Cln6^nclf* mice in the remaining retinal layers at any age: INL (Fig. 4L), IPL (Fig. 4M), and GCL (Fig. 4N). Similar changes in *Cln6^nclf* mice relative to WT controls were observed in midperipheral (Table 2) and peripheral eccentricities (Table 3). In summary, *Cln6^nclf* mice undergo a progressive reduction in photoreceptors from P60, followed by loss of the inner and outer segments, while inner retinal neurons are preserved out to P240.

## Autofluorescent Debris Accumulates in Retinal Neurons and Müller Glia of *Cln6^nclf* Mice

Autofluorescent debris, lipofuscin, has been shown to accumulate in the retina of *Cln6^nclf* mice during the retinal degeneration process[11]; however, the retinal cell types affected have not been defined. Therefore, we investigated retinal lipofuscin accumulation in more detail by imaging autofluorescence in a range of spectra (Fig. 5) and subsequently in conjunction with markers for various retinal cell types (Fig. 6). In Figure 5, images of autofluorescence from unlabeled P240 WT and *Cln6^nclf* mice in response to equal levels of laser excitation in a range of wavelengths (405, 488, 561, 633 nm) are shown. In the WT retina (Figs. 5A–D), mild levels of autofluorescence were apparent in the photoreceptor outer segments and to some extent in the outer plexiform layer, particularly when excited with the 405-nm (Fig. 5A; pseudo-colored blue), 488-nm (Fig. 5B; pseudo-colored green), and 561-nm lasers (Fig. 5C pseudo-colored red). In the *Cln6^nclf* retina (Figs. 5E–H), autofluorescent deposits were apparent as discrete pockets throughout the retina, in all retinal layers, and were best imaged using the 633-nm laser (Fig. 5H; pseudo-colored magenta), which allowed good resolution of autofluorescence in neuronal cells. As excitation with the 633-nm laser produced the least autofluorescence in the WT photoreceptors and the best resolution of lipofuscin in the *Cln6^nclf* retina, this wavelength was chosen for subsequent studies for colocalization with various retinal cell types.

Representative images of autofluorescence and a range of markers for retinal cell types at P30 and P240 in WT and *Cln6^nclf* mice are shown in Figure 6. Cone photoreceptors
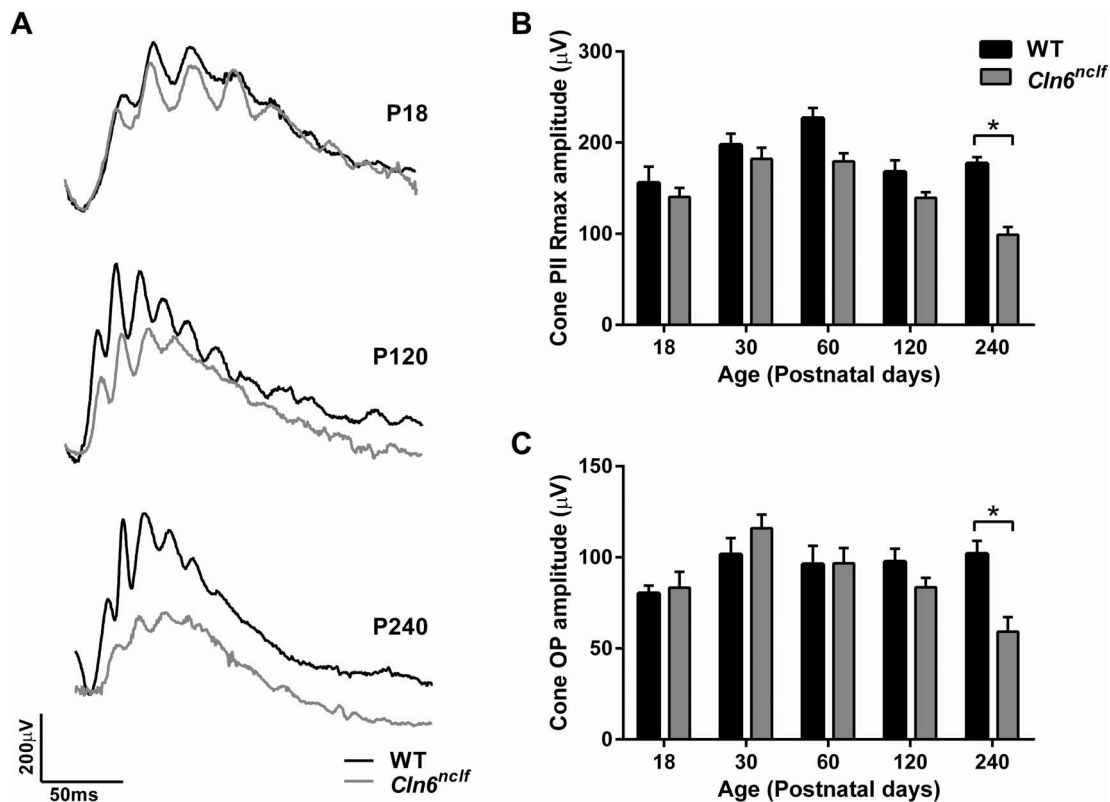
FIGURE 3. Cone pathway dysfunction occurs from postnatal day 240 in *Cln6^nclf* mice. Cone pathway function was assessed in vivo using a twin-flash ERG (flash 2.1 log cd.s/m²) in WT and *Cln6^nclf* mice at P18 through P240. (**A**) Representative cone pathway ERG waveforms are shown, highlighting loss of ERG amplitude at P240 in the *Cln6^nclf* mice (*gray line*) when compared with age-matched WT controls (*black line*). (**B**) Cone postphotoreceptor function (b-wave, PII Rmax) is reduced in *Cln6^nclf* mice at P240. (**C**) Cone postphotoreceptor OP amplitude (summed amplitudes of OPs 2–4) is reduced in *Cln6^nclf* mice at P240. All data are expressed as mean ± SEM for $n = 7$ mice at each age. Data were analyzed by a 2-way ANOVA including a Tukey multiple comparisons test with P values < 0.05 considered significant (*).
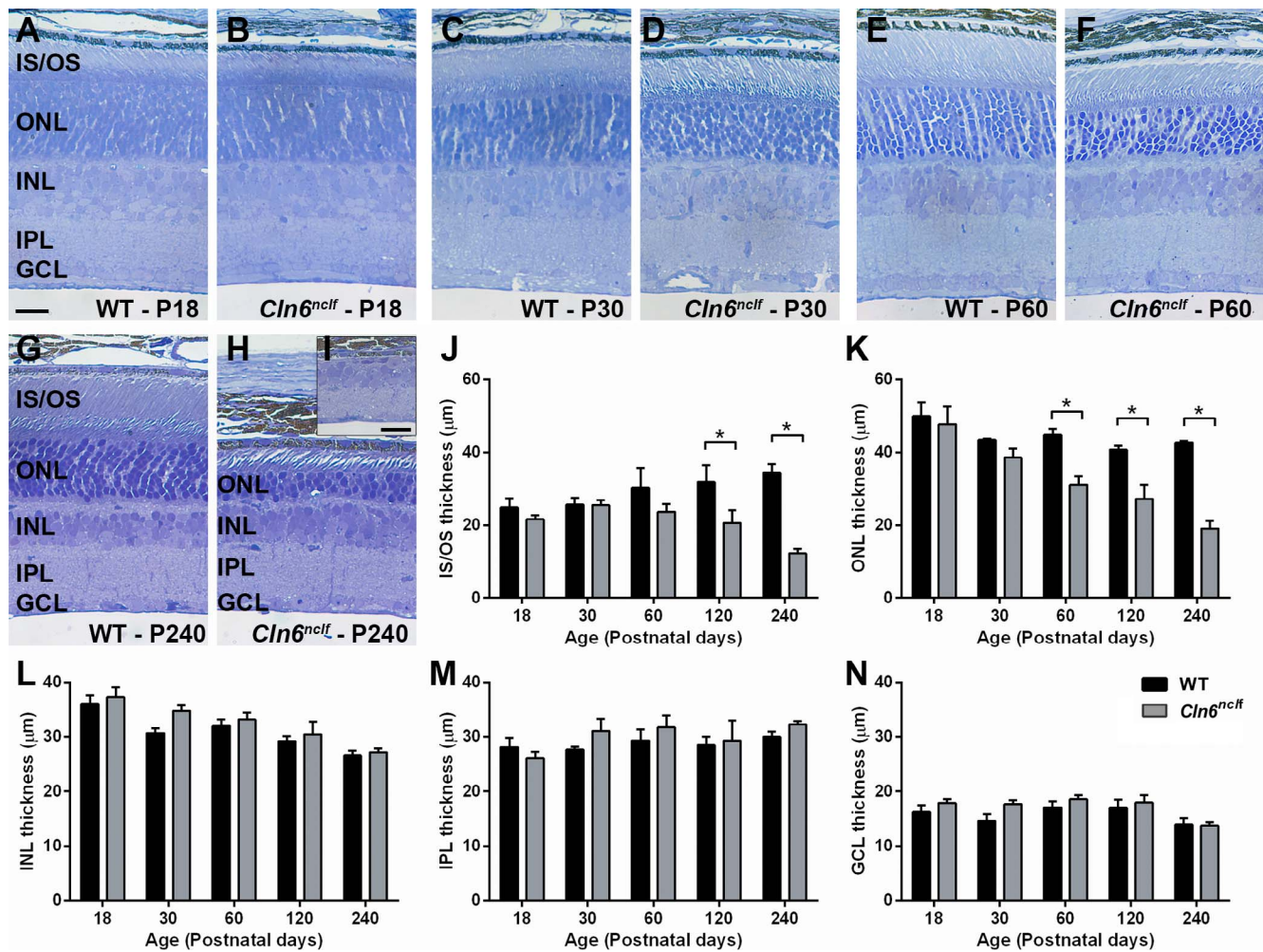
FIGURE 4. Photoreceptors degenerate from postnatal day 60 in *Cln6^{nclf}* mice while inner retinal layers are conserved. Posterior eye cups from WT and *Cln6^{nclf}* mice were collected for histologic analysis of retinal layer thickness at P18 through P240. Representative images from central retina from (**A**) WT at P18, (**B**) *Cln6^{nclf}* at P18, (**C**) WT at P30, (**D**) *Cln6^{nclf}* at P30, (**E**) WT at P60, (**F**) *Cln6^{nclf}* at P60, (**G**) WT at P240, and (**H**) *Cln6^{nclf}* at P240. (**J–N**) Images were analyzed for retinal layer thickness changes between WT and *Cln6^{nclf}* mice. (**J**) Inner segment (IS)/outer segment (OS) layer thickness was significantly reduced in *Cln6^{nclf}* mice from P120. (**K**) ONL was significantly reduced in *Cln6^{nclf}* mice from P60. (**L–N**) There were no changes in the inner retinal layers (**L**) INL, (**M**) IPL, or (**N**) GCL in *Cln6^{nclf}* compared to WT mice. All data are expressed as mean ± SEM for $n \geq 7$ mice at each age. Data were analyzed by a 2-way ANOVA including a Tukey multiple comparisons test with P values < 0.05 considered significant (*). *Scale bar*: 20 µm.

were labeled using fluorescein-bound peanut agglutinin (PNA; green) and sections imaged for autofluorescence (Auto; 633-nm excitation; pseudo-colored red) and cell nuclei (DAPI, blue; Figs. 6A–D). WT mice at P30 and P240 (Figs. 6A, 6C) showed normal cone photoreceptor labeling and no autofluorescence (Figs. 6A, 6C, respectively). At P30, *Cln6^{nclf}* mice exhibited similar PNA labeling to WT retina, and despite some rare autofluorescent deposits, there was no apparent colocalization with cone photoreceptors (Fig. 6B). However, by P240 autofluorescent debris was apparent in all retinal layers of *Cln6^{nclf}* mice, including the RPE (Fig. 6D). Furthermore, despite the loss of many photoreceptor nuclei in the ONL (see Fig. 4K), there was a relative preservation of cone numbers; however, their morphology was altered (Fig. 6D). Specifically, there was a decrease in cone inner and outer segment length (IS/OS) and occasional colocalization of autofluoresence with PNA-labeled cone photoreceptors (Fig. 6D, arrow). Amacrine and ganglion cells in WT mice at P30 and P240 showed normal calretinin labeling (CalR; green) of subsets of amacrine and ganglion cells and no autofluorescence (red; Fig. 6E, 6G, respectively). While

colocalization of calretinin and lipofuscin was absent in P30 *Cln6^{nclf}* mice (Fig. 6F), autofluorescent deposits within intact amacrine and ganglion cells were apparent at P240 (Fig. 6H, arrow in magnified inset Hi). Retinal Müller cells were labeled using an antibody against glutamine synthetase (GS; green; Figs. 6I–J). At P240, Müller glia displayed normal morphology in WT retina (Fig. 6I); however, in *Cln6^{nclf}* mice, isolated autofluorescent deposits were apparent within Müller cells adjacent to cell nuclei (Fig. 6J, arrow in magnified inset Ji). Despite this accumulation of autofluorescent debris, there was no effect on cell survival, as Müller cell number did not change between WT and *Cln6^{nclf}* mice at this age (Fig. 6K). In summary, at P240, there was a distinct thinning of the photoreceptor layers in *Cln6^{nclf}* mice; however, lipofuscin accumulation was apparent throughout the retina and had little adverse effect on retinal structure and cellular survival of the inner retinal cell types investigated, including amacrine cells, ganglion cells, and Müller glia.

TABLE 2. Retinal Layer Thickness Measurements for the Midperiphery. Data Presented as Mean (μm) ± SEM for $n = 5$ or 6 Retinae From WT and *Cln6^nclf* Mice of Each Postnatal Age

Layer, Postnatal Day	WT		*Cln6^nclf*		*P* Value
	Average	SEM	Average	SEM	
GCL					
P18	13.98	2.21	13.33	0.49	0.61
P30	10.43	0.51	13.20	0.74	0.32
P60	12.25	0.92	11.96	0.76	0.83
P120	11.09	0.75	11.92	0.35	0.54
P240	10.76	0.92	10.24	0.35	0.69
IPL					
P18	24.87	2.38	24.82	1.68	0.98
P30	23.38	0.45	27.79	2.12	0.07
P60	27.86	2.22	28.09	1.54	0.93
P120	26.85	1.71	25.57	3.13	0.63
P240	27.09	1.13	28.11	0.99	0.69
INL					
P18	33.88	3.18	36.63	1.81	0.23
P30	29.56	0.68	32.91	1.29	0.15
P60	30.65	1.19	31.58	1.17	0.71
P120	28.39	1.48	31.09	2.53	0.28
P240	25.98	1.65	25.02	1.03	0.69
ONL					
P18	43.39	2.88	45.15	1.51	0.44
P30	38.91	1.11	36.65	1.54	0.32
P60	41.61	1.53	29.80	1.62	<0.0001
P120	39.01	1.22	28.72	2.94	0.0001
P240	43.14	1.06	20.85	0.73	<0.0001
IS/OS					
P18	23.00	1.21	21.05	1.38	0.40
P30	25.08	0.78	22.49	1.70	0.27
P60	30.39	1.94	23.85	0.78	0.01
P120	30.89	1.92	21.76	3.90	0.001
P240	36.02	1.85	13.83	0.84	<0.0001
Total					
P18	116.12	10.51	119.93	5.24	0.62
P30	102.28	1.64	110.55	5.36	0.28
P60	112.37	5.42	101.43	4.46	0.19
P120	105.34	4.82	97.30	8.81	0.33
P240	106.97	3.58	84.21	2.44	0.01

TABLE 3. Retinal Layer Thickness Measurements for the Periphery. Data Presented as Mean (μm) ± SEM for $n = 5$ or 6 Retinae From WT and *Cln6^nclf* Mice of Each Postnatal Age

Layer, Postnatal Day	WT		*Cln6^nclf*		*P* Value
	Average	SEM	Average	SEM	
GCL					
P18	10.30	0.98	11.16	0.73	0.28
P30	8.07	0.18	9.61	0.63	0.09
P60	8.63	0.39	8.58	0.62	0.95
P120	8.41	0.45	8.66	0.70	0.78
P240	8.01	0.59	6.94	0.51	0.21
IPL					
P18	20.30	1.67	21.92	1.71	0.47
P30	17.72	1.15	22.22	1.77	0.15
P60	23.24	2.72	21.45	1.44	0.46
P120	20.49	1.74	19.54	1.52	0.70
P240	21.97	1.66	21.03	1.40	0.68
INL					
P18	29.05	2.97	33.02	2.50	0.08
P30	22.56	0.81	26.79	1.30	0.07
P60	25.18	1.71	24.68	1.35	0.84
P120	23.92	1.19	21.81	1.29	0.40
P240	21.77	1.92	19.50	0.93	0.34
ONL					
P18	39.84	2.48	42.33	1.61	0.23
P30	32.46	1.43	31.18	1.45	0.54
P60	34.25	1.39	22.30	1.86	<0.0001
P120	33.47	1.15	18.91	1.67	<0.0001
P240	36.63	1.53	11.69	0.88	<0.0001
IS/OS					
P18	18.97	0.55	17.83	1.75	0.47
P30	20.84	1.04	18.54	0.69	0.15
P60	24.67	1.71	17.74	1.18	0.0002
P120	24.65	1.32	13.35	1.13	<0.0001
P240	29.97	1.49	5.75	0.77	<0.0001
Total					
P18	99.49	7.96	108.44	6.32	0.19
P30	80.80	2.46	89.80	4.90	0.19
P60	91.30	6.04	77.01	4.88	0.06
P120	86.29	4.10	68.92	4.93	0.02
P240	88.39	5.13	59.16	3.16	0.00

Autophagy–Lysosomal Pathways Are Impaired in the Photoreceptor Layers but Not in the RPE or Inner Retina in *Cln6^nclf* Mice at Postnatal Day 30

Disturbances in lysosomal degradation within the RPE have been implicated to play a role in the formation of lipofuscin and subsequent photoreceptor death of the *Cln3* mouse model.[16] To determine whether changes in the RPE, photoreceptors, or both contribute to photoreceptor loss in *Cln6^nclf* mice, the autophagy–lysosomal pathways were assessed in WT and *Cln6^nclf* mice at P30 (Fig. 7), a time when photoreceptors are dysfunctional but gross cellular structure is intact. Sections were labeled with anti-microtubule associated protein light chain 3 isoform B (LC3; red) for autophagosomes and anti-lysosomal associated membrane protein 1 (LAMP1; green) for lysosomes. In the RPE, autophagosome and lysosome distribution, average size, and their colocalization were similar in WT (Fig. 7A) and *Cln6^nclf* mice (Fig. 7B). In contrast to the RPE, separation of the photoreceptor layer into OS/IS (Figs. 6C, 6D) and nuclei (ONL; Figs. 7E, 7F) showed changes in the number and size of autophagosomes and lysosomes in the subcompartments of this layer in the *Cln6^nclf* mice. In the INL, there were

no distinct differences in LC3 or LAMP1 labeling between WT (Fig. 7G) and *Cln6^nclf* mice (Fig. 7H).

LC3-positive autophagosomes and LAMP1-positive lysosome number (puncta number/area of region of interest, μm²) and average puncta size (μm²), as well as colocalization of autophagosomes and lysosomes, were quantified for each retinal layer in WT and *Cln6^nclf* mice (Figs. 7I–L). The number of LC3-positive autophagosomes was significantly reduced in the photoreceptor layers, IS/OS, and ONL of *Cln6^nclf* (gray) relative to WT mice (black), but no significant changes were apparent in the RPE or INL (Fig. 7I). Similarly, the number of LAMP1-postive lysosomes was not different in the RPE and INL between *Cln6^nclf* and WT mice; however, there was a significant decrease in lysosome number in the IS/OS and an increase in number in the ONL of *Cln6^nclf* mice (Fig. 7J). Colocalization of LC3-positive autophagosomes with LAMP1-positive puncta was significantly reduced in the photoreceptor layers, IS/OS, and ONL of *Cln6^nclf* relative to WT mice, but there was no change in the RPE or INL of *Cln6^nclf* at this stage (Fig. 7K). In addition, LC3-positive autophagosomes and LAMP1-positive lysosomes were significantly larger in the ONL of *Cln6^nclf* relative to WT mice (Fig. 7L), but not in the other layers (data not shown). These data suggest that
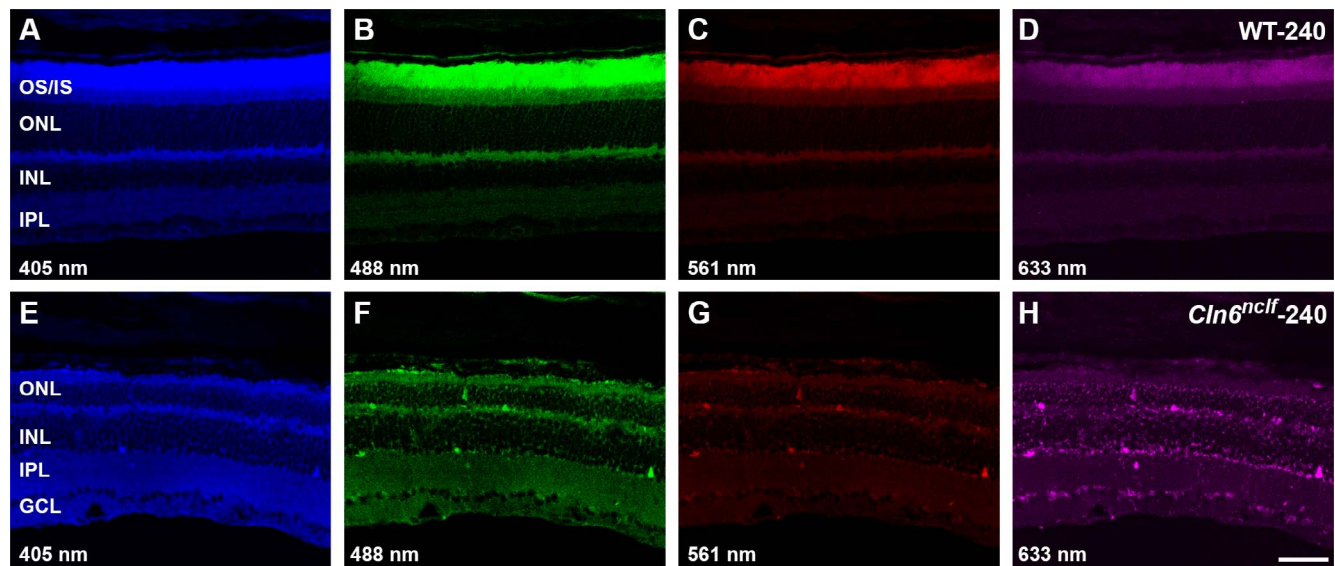
FIGURE 5. Autofluorescent debris within retinal neurons localized using laser confocal imaging in WT and $Cln6^{nclf}$ mice at postnatal day 240. Transverse retinal sections from WT and $Cln6^{nclf}$ mice were collected for histologic analysis and imaged using confocal microscopy for autofluorescence. (**A–D**) Retina from a WT mouse at P240 imaged under ×20 magnification using laser wavelengths (**A**) 405 nm, pseudo-colored *blue*, (**B**) 488 nm, pseudo-colored *green*, (**C**) 561 nm, pseudo-colored *red*, (**D**) 633 nm, pseudo-colored *magenta*. (**E–H**) In the $Cln6^{nclf}$ retina, autofluorescent deposits were apparent as discrete pockets throughout the retina, in all retinal layers, and were apparent under (**A**) 405-nm, (**B**) 488-nm, (**C**) 561-nm lasers but were best imaged using the (**H**) 633-nm laser. *Scale bar*: 20 μm (**A–G**).

autophagy commencement and lysosomal degradation are reduced in the photoreceptor layers but not in the RPE or inner retina in the $Cln6^{nclf}$ mouse at P30.

LC3-II and P62 Accumulate in $Cln6^{nclf}$ Retina and in WT Retina Treated With the Autophagy–Lysosomal Degradation Blocker Chloroquine at Postnatal Day 30

To further investigate autophagy–lysosomal pathways at P30, retina from WT and $Cln6^{nclf}$ mice were incubated overnight in culture media in the absence (−) and presence (+) of 50 μM chloroquine and the next day prepared for analysis by Western blot for LC3 (Figs. 8A, 8B) and P62 (Figs. 8C, 8D). Western blot bands from 2 of $n = 5$ eyes sampled for each group are presented as examples. In WT retina under control conditions, LC3-II expression was low relative to LC3-I; however, in the presence of the autophagy–lysosomal degradation blocker, chloroquine, LC3-II levels increased relative to LC3-I (Fig. 8A), and this change was significant (Fig. 8B; WT control versus WT chloroquine; #$P < 0.05$). In $Cln6^{nclf}$ retina, LC3-II levels were consistently high relative to LC3-I (Fig. 8A) and were higher than in the WT control, and treatment with chloroquine had no further effect on this ratio (Fig. 8B; $Cln6^{nclf}$ control versus WT control, *$P < 0.05$, and $Cln6^{nclf}$ chloroquine versus WT chloroquine, *$P < 0.05$; $Cln6^{nclf}$ control versus $Cln6^{nclf}$ chloroquine, not significant $P = 0.27$). Similarly, analysis of P62 showed that chloroquine enhanced deposition of debris tagged for autophagic degradation in WT retina (Fig. 8C), and this change was significant (Fig. 8D; WT control versus WT chloroquine, #$P < 0.05$). P62 expression levels were high in $Cln6^{nclf}$ retina (Fig. 8C) relative to WT retina and were further increased by treatment with chloroquine (Fig. 8D; $Cln6^{nclf}$ control versus WT control, *$P < 0.05$; $Cln6^{nclf}$ control versus $Cln6^{nclf}$ chloroquine, #$P < 0.05$). These data suggest that at

P30, when cell loss in the retina is not yet significant, retinal autophagy–lysosomal degradation pathways are impeded but not completely blocked in $Cln6^{nclf}$ mice.

The Waste Aggregate Tag P62 Accumulates in the Cytosol, and the Mitochondrial Protein ATP Synthase Subunit C Accumulates in the Lysosomes of Photoreceptors in $Cln6^{nclf}$ Mice at Postnatal Day 30

As lysosomal degradation in the photoreceptor nuclear layer was disturbed in $Cln6^{nclf}$ mice at P30, accumulation of undigested protein/waste aggregates and mitochondrial proteins was assessed histologically in WT and $Cln6^{nclf}$ mice at P30 (Fig. 9). Aggregated cellular debris tagged for autophagic degradation, labeled by P62/SQSTM1 (green), was very low in WT photoreceptors and RPE as P62 is degraded in the autophagy process (Fig. 9A). In contrast, P62 accumulation was apparent in the cytosol of the photoreceptor layers in $Cln6^{nclf}$ mice (Fig. 9B). In the RPE, P62 aggregates were occasionally apparent but were qualitatively infrequent, suggesting that like the LC3-LAMP1 assessment (Fig. 7), autophagy processes involving P62 are less affected in the RPE relative to the photoreceptors in $Cln6^{nclf}$ mice at P30. Mitochondria and their degradation/recycling were also investigated (Figs. 9C–H). While there were no obvious changes observed over several images in the morphology, frequency, and distribution of mitochondria (MTCO1, green) in the photoreceptor layers between WT controls (Fig. 9C) and $Cln6^{nclf}$ mice (Fig. 9D), there were changes in the degradation and recycling of mitochondrial proteins. The mitochondrial degradative product ATP synthase subunit C (ATPsyn; red) could not be detected in the WT retina, as like P62, it is readily digested in the autophagy–lysosomal recycling process (Fig. 9E). However, photoreceptors of $Cln6^{nclf}$ mice showed accumulation of this mitochondrial protein (red), commonly colocalized with lysosomes (green; Fig. 9F, inset magnified in Fig. 9Fi). In the RPE of $Cln6^{nclf}$ mice also, ATPsynthase subunit
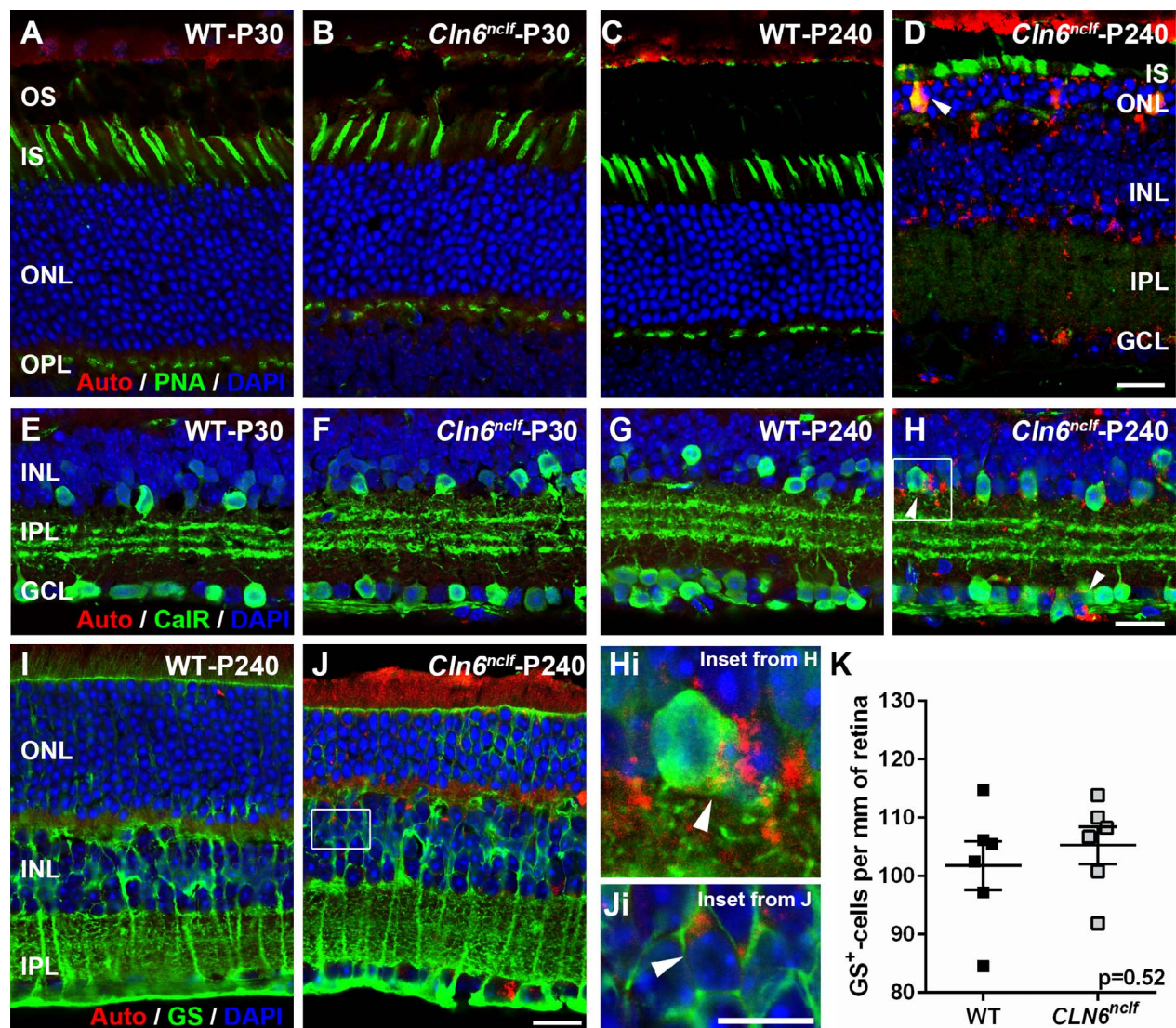
FIGURE 6. All retinal neurons and Müller glia accumulate autofluorescent debris in *Cln6^nclf* mice. Transverse retinal sections from WT and *Cln6^nclf* mice were collected for histologic analysis and imaged using confocal microscopy for autofluorescent debris within various retinal cell types. (**A–D**) Retinae from (**A**) WT at P30, (**B**) *Cln6^nclf* mice at P30, (**C**) WT at P240, and (**D**) *Cln6^nclf* mice at P240 were imaged for cone photoreceptors (PNA, *green*), autofluorescence (633-nm laser, pseudo-colored *red*), and cell nuclei (DAPI, *blue*). At P240, *Cln6^nclf* mice showed accumulation of autofluorescent debris in all cell types, including cone photoreceptors (*arrow*). (**E–H**) Retinae from (**E**) WT at P30, (**F**) *Cln6^nclf* mice at P30, (**G**) WT at P240, and (**H**) *Cln6^nclf* mice at P240 were imaged for amacrine and ganglion cells (calretinin, CalR, *green*), autofluorescence (*red*), and cell nuclei (DAPI, *blue*). (**H, Hi**) At P240, *Cln6^nclf* mice showed accumulation of autofluorescent debris in inner retinal neurons, including amacrine cells (*arrow, Hi*). (**I–J**) Retinae from (**I**) WT at P240 and (**J**) *Cln6^nclf* mice at P240 were imaged for Müller glia (glutamine synthetase, GS, *green*), autofluorescence (*red*), and cell nuclei (DAPI, *blue*). (**J, Ji**) At P240, *Cln6^nclf* mice showed accumulation of autofluorescent debris in Müller glia (*arrow* in **Ji**). (**K**) There were no changes in the number of GS-positive Müller glia between WT and *Cln6^nclf* mice at P240. Data are expressed as mean ± SEM for $n \geq 5$ mice and were analyzed by a Student's *t*-test. *Scale bar*: 20 μm (**A–Ji**).

C was found to accumulate relative to WT RPE (Figs. 9G, 9H; 9G, WT; 9H, *Cln6^nclf*), suggesting alterations in mitochondrial processing is an early and ubiquitous marker of cellular changes in ocular tissues in *Cln6^nclf* mice.

DISCUSSION

Decline in vision caused by retinal accumulation of lipofuscin and photoreceptor death represents one of the first symptoms in infantile and childhood NCL forms.[2,30] In the *Cln6^nclf* mouse model of late-infantile NCL there was a significant loss of rod photoreceptor function at P18, prior to photoreceptor nuclei loss at P60. In contrast, postphotoreceptor rod and cone pathway function were not affected until P120 and P240, respectively. The loss of rod photoreceptor function correlated with significant disruption of the autophagy–lysosomal degradation pathways within photoreceptors at P30, a time when there were no significant changes in the RPE or other retinal neurons. At P30 also there was cytosolic accumulation of P62 as well as extensive colocalization of undigested ATP synthase subunit C within lysosomes of *Cln6^nclf* mice. These results suggest that rod photoreceptor cells have an increased sensitivity to disturbances in the autophagy–lysosomal pathway and the subsequent failure of mitochondrial turnover, relative to other retinal cells. It is likely that primary failure of the photoreceptors rather than the RPE or other retinal
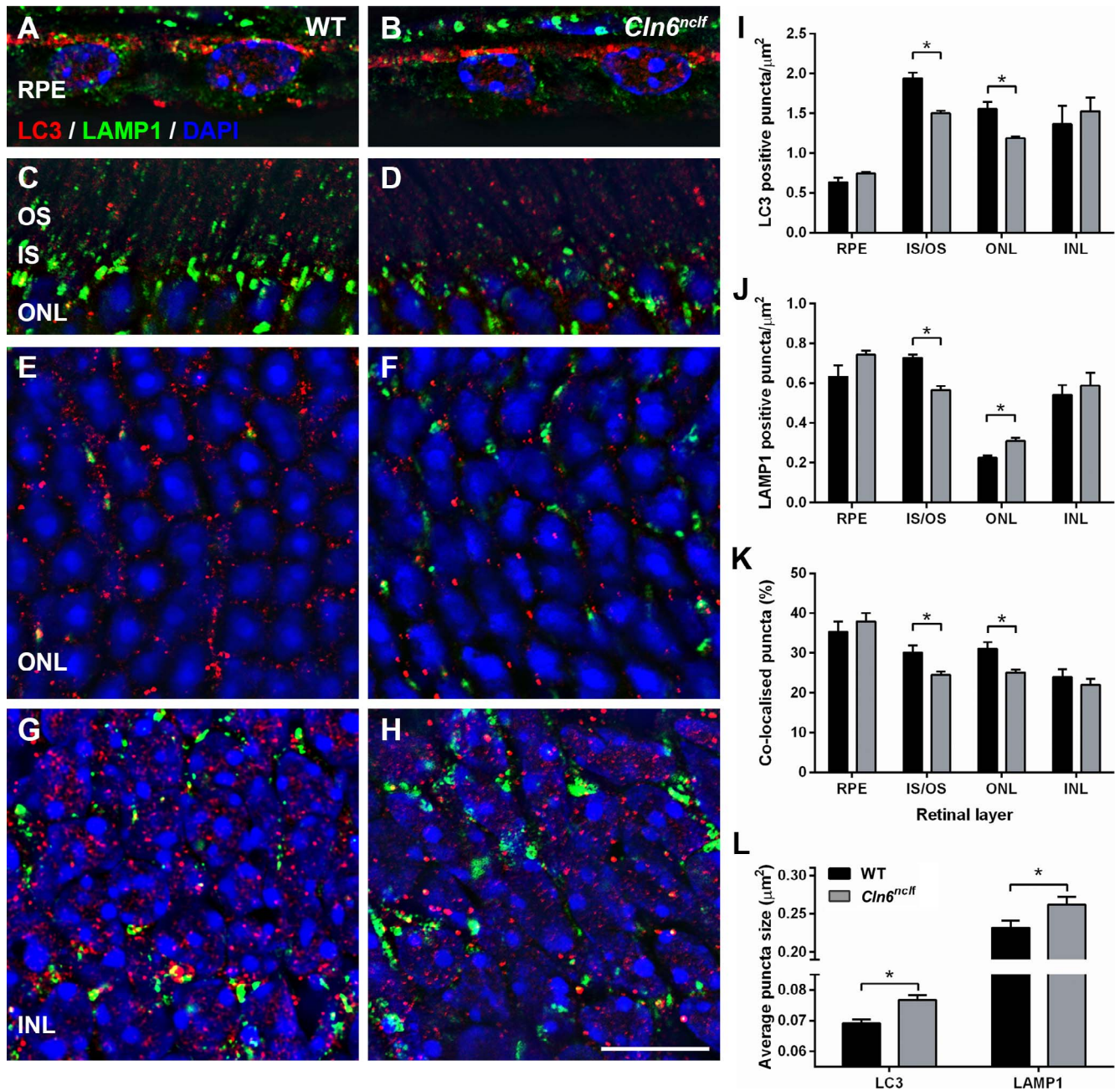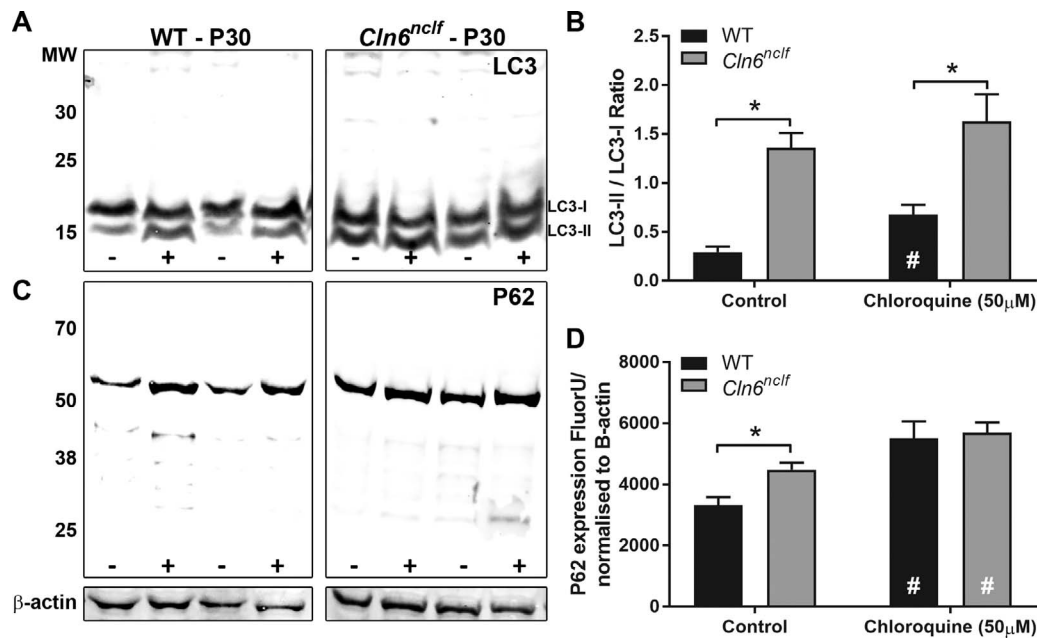
FIGURE 7. At postnatal day 30, autophagy–lysosomal pathways are dysfunctional in the photoreceptor layers of *Cln6*^{nclf} mice. Transverse retinal sections from P30 WT and *Cln6*^{nclf} mice were collected for histologic analysis and imaged using confocal microscopy for autophagosomes (LC3B, *red*), lysosomes (LAMP1, *green*), and cell nuclei (DAPI, *blue*). (**A, B**) RPE layer from (**A**) WT and (**B**) *Cln6*^{nclf} mice. (**C, D**) Photoreceptor OS/IS layers from (**C**) WT and (**D**) *Cln6*^{nclf} mice. (**E, F**) Photoreceptor nuclei in the ONL from (**E**) WT and (**F**) *Cln6*^{nclf} mice. (**G, H**) The INL from (**G**) WT and (**H**) *Cln6*^{nclf} mice. (**I**) Quantification of LC3-positive puncta in each retinal layer for WT (*black*) and *Cln6*^{nclf} mice (*gray*). (**J**) Quantification of LAMP1-positive puncta in each retinal layer for WT (*black*) and *Cln6*^{nclf} mice (*gray*). (**K**) Quantification of colocalized LC3-positive puncta as a percentage of LAMP1-postive puncta in each retinal layer for WT (*black*) and *Cln6*^{nclf} mice (*gray*). (**L**) The area of LC3-positive and LAMP1-positive puncta was assessed in each retinal layer and data for the outer nuclear layer are shown. Data are expressed as mean $\pm$ SEM for $n \geq 5$ mice and were analyzed by a 2-way ANOVA, including a Tukey multiple comparisons test with P values < 0.05 considered significant (*). *Scale bar*: 20 μm (**A–H**).

neurons underlies the early visual dysfunction that occurs in the *Cln6*^{nclf} mouse model.

Lipofuscin accumulation within postmitotic cells is a key characteristic of NCL, and in humans, retinal deposits are apparent as reflective lesions in the fundus of infantile NCL patients.[31] In *Cln6*^{nclf} mice, white fundus lesions were apparent from 2 months of age (P60) and these increased in number across all quadrants of the eye with age. Currently, the origin of these fundus lesions in mice is unclear. Some studies

suggest these types of lesions correlate with the accumulation of lipofuscin primarily in the RPE.[32,33] Others studies suggest that infiltrating macrophages, which are autofluorescent, are responsible for this phenomenon,[34,35] and while resident retinal microglia are active by 1 month of age in *Cln6*^{nclf} mice,[11] fundus images have not been published previously. It is likely that in *Cln6*^{nclf} mice, the fundus lesions represent a combination of both autofluorescent retinal macrophages and

FIGURE 8. LC3-II and P62 accumulate in *Cln6^nclf* retina and in WT retina treated with the autophagy–lysosomal degradation blocker chloroquine at postnatal day 30. Autophagy–lysosomal pathways were assessed by Western blot for LC3 (**A**, **B**) and P62 (**C**, **D**) from whole retinae from WT and *Cln6^nclf* mice at P30 that were incubated overnight in culture media in the absence (−) and presence (+) of 50 μM chloroquine. (**A**) LC3 Western blot bands from 2 of $n = 5$ eyes sampled for each group are presented as examples. (**B**) In WT retinae under control conditions, LC3-II expression was low relative to LC3-I; however, in the presence of the autophagy–lysosomal degradation blocker, chloroquine, LC3-II levels increased relative to LC3-I (WT control versus WT chloroquine; #$P < 0.05$). In *Cln6^nclf* retina, LC3-II levels were consistently high relative to LC3-I and treatment with chloroquine had no further effect on this ratio (*Cln6^nclf* control versus WT control, *$P < 0.05$; *Cln6^nclf* chloroquine versus WT chloroquine, *$P < 0.05$; *Cln6^nclf* control versus *Cln6^nclf* chloroquine, not significant $P = 0.27$). (**C**) P62 Western blot bands from 2 of $n = 5$ eyes sampled for each group are presented as examples. (**D**) Analysis of P62 expression showed chloroquine treatment enhanced P62 levels in WT retina (WT control versus WT chloroquine; #$P < 0.05$). P62 expression levels were high in *Cln6^nclf* retina relative to WT retina and were further increased by treatment with chloroquine (*Cln6^nclf* control versus WT control, *$P < 0.05$; *Cln6^nclf* control versus *Cln6^nclf* chloroquine, #$P < 0.05$). Data are expressed as mean ± SEM for $n = 5$ retinae/treatment group and were analyzed by a 2-way ANOVA for genotype and chloroquine treatment including a Tukey multiple comparisons test with P values < 0.05 considered significant between genotype (*) and between chloroquine +/− treatment (#).

cellular lipofuscin accumulation as has been shown to occur in other mouse models previously.[20,21]

Histologic analysis showed that there was accumulation of autofluorescent lipofuscin within retinal neurons from P30 and that these deposits increased with age in *Cln6^nclf* mice. These autofluorescent deposits were best imaged using 633-nm wavelength laser, suggesting their origin may be different from A2E deposition, which has previously been suggested to be best imaged with 488-nm excitation[36] and an emission maxima of 565 to 570.[37] In any case, the finding that autofluorescent deposits accumulate from P30 in *Cln6^nclf* mice is consistent with recent studies, which show that lipofuscin accumulation occurs with age in the retina of *Cln6^nclf* mice,[10,11] as well in the *Cln3* mouse model of juvenile NCL.[38] In the present study, accumulation of lipofuscin was apparent in all retinal cell types of *Cln6^nclf* mice, but only rod photoreceptors were affected initially, with significant functional deficits apparent at P18 and cellular loss apparent from P60. While loss of rod photoreceptor function and number has been observed in previous studies of *Cln6^nclf* mice[10,11] as well as *Cln8*[39] and other forms of NCL,[38,40,41] these previous studies did not carefully investigate other neuronal classes. The present study shows that rod photoreceptors are affected first, while other retinal neuronal classes including cone photoreceptors are spared despite accumulation of autofluorescent lipofuscin in the RPE and all retinal neurons. For example, cone pathway function and the number of cone photoreceptors were not affected until P240 (8 months), and even at this stage, cone numbers were still relatively plentiful in the central retina. Also, in the inner retina, while amacrine cell function was affected from P120, amacrine cell structure was intact up to P240 despite accumulation of lipofuscin in amacrine cells. This suggests a primary failure of the rod photoreceptors themselves or a failure of nonneural retinal support cells (RPE) as contributing to the retinal degeneration phenotype observed in *Cln6^nclf* mice.

We directly addressed this question of whether the rod photoreceptor and/or RPE contribute to degeneration in the *Cln6^nclf* model. Overall, the results of the autophagy–lysosomal pathway analysis suggest that a primary dysfunction within photoreceptor cells is the likely cause of rod photoreceptor degeneration in *Cln6^nclf* mice. At P30, autophagy–lysosomal function was significantly impaired within the photoreceptor cell bodies and inner segments; however, no changes were observed in the INL or in the RPE at this age. Specifically, there was a decrease in autophagosomal–lysosomal fusion events, likely leading to an increased size of both autophagosome and lysosome vesicles in the photoreceptors of *Cln6^nclf* mice. This present finding is in contrast to studies of autophagy processes in *Cln3^Δex1-6* mice, which suggest that RPE dysfunction may underlie retinal degeneration in this model.[16] In the *Cln3^Δex1-6* mice, accumulation of ATP synthase subunit C was present in the brain and RPE. This was found to occur as a result of insufficient autophagosomal–lysosomal fusion leading to a decreased degradation of phagosome contents in the RPE.[16] However, retinal changes were not carefully characterized and cannot be discounted. In the *Cln5* mouse model also, changes in autophagy (ratio of LC3I to II) were observed generally in the retina, but the RPE was also suggested to play an important role in retinal degeneration in this model.[17]
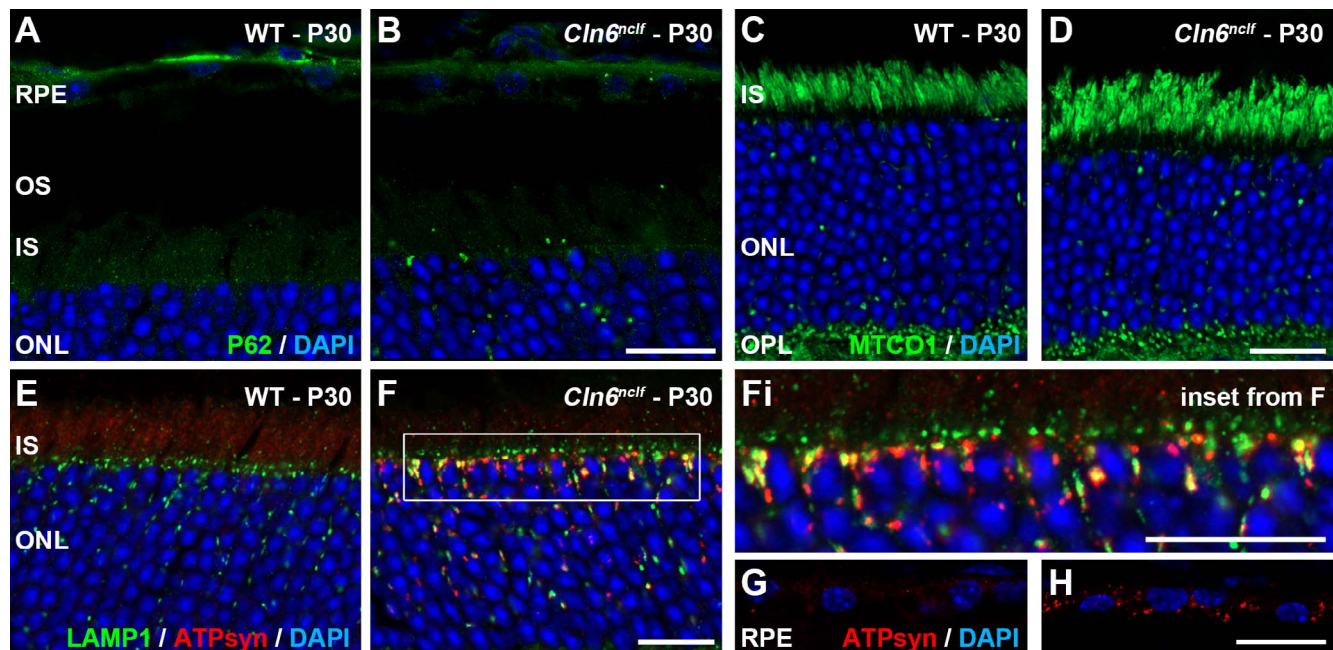
FIGURE 9. At postnatal day 30, P62-tagged proteins aggregate in the cytosol and undigested mitochondrial proteins accumulate in lysosomes in the photoreceptor layers of *Cln6^nclf* mice. Transverse retinal sections from P30 WT and *Cln6^nclf* mice were collected for histologic analysis and imaged using confocal microscopy for autophagy–lysosomal and mitochondrial proteins and cell nuclei (DAPI, *blue*). (**A, B**) RPE, photoreceptor OS/IS, and ONL from (**A**) WT and (**B**) *Cln6^nclf* mice were labeled for P62/SQSTM1-tagged protein aggregates (P62, *green*). P62 labeling was absent in WT retina, but P62-tagged undigested waste was apparent in *Cln6^nclf* retina. (**C, D**) Photoreceptor OS/IS and ONL from (**C**) WT and (**D**) *Cln6^nclf* mice were labeled for mitochondria with an antibody against mitochondrial complex IV subunit I (MTCO1, *green*). (**E, F**) Photoreceptor OS/IS and ONL from (**E**) WT and (**F**) *Cln6^nclf* mice were labeled for the mitochondrial degradation product, ATP synthase C (ATPsyn, *red*). ATP synthase was absent in the WT retina as it is normally degraded efficiently in lysosomes (LAMP1, *green*). (**Fi**) Magnified view of inset from (**F**), showing ATP synthase C accumulates within lysosomes in *Cln6^nclf* mice. (**G, H**) RPE from (**G**) WT and (**H**) *Cln6^nclf* mice were labeled for the mitochondrial degradation product, ATP synthase C (ATPsyn, *red*) and cell nuclei (DAPI, *blue*). ATP synthase accumulation was elevated in the RPE of *Cln6^nclf* mice. *Scale bar*: 20 μm (**A–H**).

Our functional and immunocytochemical data also support our autophagy–lysosomal pathway analysis suggesting that RPE dysfunction is unlikely to be the primary driver of rod photoreceptor death, as with RPE failure, both rod and cone photoreceptors might have been expected to deteriorate, and instead cone photoreceptor function remained relatively stable up until P240. Also, there were no early histologic changes in autophagy–lysosomal pathways in the RPE of *Cln6^nclf* mice that may have contributed to rod photoreceptor dysfunction at P30. While we saw global retinal changes in the autophagy–lysosomal degradation process in *Cln6^nclf* retina, one advantage of the histologic approach taken here, as opposed to total retinal or RPE protein quantifications using Western blot described herein and in previous studies,[17] is that in this study the use of super-resolution microscopy allowed quantification of changes in autophagy on a cellular level. Thus, at P30, a time when photoreceptor nuclei remained but rods were dysfunctional, reductions in autophagosomes and autophagy–lysosomal fusion events were apparent specifically within photoreceptors and not other cell types, suggesting that this cell type is particularly sensitive to autophagy–lysosomal dysregulation. This suggestion is supported by findings in a mouse model in which autophagy is selectively blocked in rod photoreceptors by deletion of Atg5; this mouse shows a similar retinal degeneration phenotype to the *Cln6^nclf* mouse, in terms of disruption of autophagy–lysosomal degradation and subsequent photoreceptor loss.[28]

Further investigation of the photoreceptors at P30 showed that there was abnormal accumulation of P62 and the mitochondrial-derived protein, ATP synthase subunit C, in *Cln6^nclf* mice. P62 plays an important role in tagging aggregated proteins for intracellular digestion and the antioxidant response,[42] and it has been shown to accumulate in neurons of various NCL models.[7,43] Accumulation of P62 in photoreceptors in *Cln6^nclf* mice at P30 suggests that incomplete loading of autophagosomes and insufficient degradation of protein aggregates (aggrephagy) are occurring at this time. In addition, colocalization of ATP synthase subunit C with lysosomes was apparent in photoreceptors in *Cln6^nclf* mice but not in WT mice. This phenomenon has been seen in the brain and other tissues of various models of NCLs[44–47] and suggests that failure of mitochondrial degradation (mitophagy) is occurring in *Cln6^nclf* mice. As the retina and in particular, photoreceptors, have one of the greatest energy requirements of the entire body, they would be extremely sensitive to failures in energy production due to dysregulation of mitochondrial turnover. While it has been suggested that photoreceptor energy requirements are mostly glycolytic,[48] photoreceptor inner segments are densely packed with mitochondria, perhaps to buffer calcium[49] but also perhaps to meet high metabolic demands[50,51] such as maintaining photoreceptor depolarization, the photoreceptor dark current.[51] Therefore, one reason that rod photoreceptors may be primarily affected in *Cln6^nclf* mice may be failure of mitochondrial turnover, insufficient energy production, and reduced intracellular calcium buffering capacity. This begs the question why rod photoreceptors may be affected prior to cone photoreceptors. In the mouse, rod and cone photoreceptors have differences in mitochondrial structure and number and metabolism, which may afford cone photoreceptors protection against metabolic insults.[52] Additionally, mouse cone photoreceptors have shorter outer segments, much larger inner segments, larger

axon diameter (1.4 μm in cones versus 0.35 μm in rods), and larger terminals,[53] which may potentially provide additional cytoplasmic storage for lysosomal accumulations when compared with rods. It is possible that these metabolic and morphologic differences allow cones to be more resilient to autophagy–lysosomal dysfunction; however, more work is required to determine why rod pathway dysfunction precedes cone pathway dysfunction in *Cln6*^{nclf} mice.

In conclusion and in summary, this study provides detailed evidence suggestive of primary photoreceptor failure and death as the likely mechanism underlying retinal degeneration in the *Cln6*^{nclf} mouse model. Rod photoreceptor death likely occurs due to a significant decrease of autophagosomal–lysosomal fusion events within photoreceptor cells and failure of lysosomal degradation, accompanied by early cytosolic accumulation of aggregated proteins. Furthermore, in comparison to other prevalent retinal diseases such as AMD and Stargardt's disease, which are also characterized by lipofuscin accumulation, our findings in *Cln6*^{nclf} mice show a different pathomechanism, as critical functions of the RPE were not affected early in the disease process in *Cln6*^{nclf} mice.[54–56] Future studies investigating therapies for retinal degeneration in *Cln6*^{nclf} mice should therefore target photoreceptors to ameliorate or slow visual decline in this disorder.

Acknowledgments

References

1. Jalanko A, Braulke T. Neuronal ceroid lipofuscinoses. *Biochim Biophys Acta*. 2009;1793:697–709.

2. Haltia M. The neuronal ceroid-lipofuscinoses: from past to present. *Biochim Biophys Acta*. 2006;1762:850–856.

3. Mole SE, Williams RE, Goebel HH. Correlations between genotype, ultrastructural morphology and clinical phenotype in the neuronal ceroid lipofuscinoses. *Neurogenetics*. 2005;6:107–126.

4. Warrier V, Vieira M, Mole SE. Genetic basis and phenotypic correlations of the neuronal ceroid lipofusinoses. *Biochim Biophys Acta*. 2013;1832:1827–1830.

5. Heine C, Koch B, Storch S, Kohlschutter A, Palmer DN, Braulke T. Defective endoplasmic reticulum-resident membrane protein CLN6 affects lysosomal degradation of endocytosed arylsulfatase A. *J Biol Chem*. 2004;279:22347–22352.

6. Holopainen JM, Saarikoski J, Kinnunen PK, Jarvela I. Elevated lysosomal pH in neuronal ceroid lipofuscinoses (NCLs). *Eur J Biochem*. 2001;268:5851–5856.

7. Thelen M, Damme M, Schweizer M, et al. Disruption of the autophagy-lysosome pathway is involved in neuropathology of the nclf mouse model of neuronal ceroid lipofuscinosis. *PLoS One*. 2012;7:e35493.

8. Gao H, Boustany RM, Espinola JA, et al. Mutations in a novel CLN6-encoded transmembrane protein cause variant neuronal ceroid lipofuscinosis in man and mouse. *Am J Hum Genet*. 2002;70:324–335.

9. Mole SE, Michaux G, Codlin S, Wheeler RB, Sharp JD, Cutler DF. CLN6, which is associated with a lysosomal storage disease, is an endoplasmic reticulum protein. *Exp Cell Res*. 2004;298:399–406.

10. Bartsch U, Galliciotti G, Jofre GF, Jankowiak W, Hagel C, Braulke T. Apoptotic photoreceptor loss and altered expression of lysosomal proteins in the nclf mouse model of neuronal ceroid lipofuscinosis. *Invest Ophthalmol Vis Sci*. 2013;54:6952–6959.

11. Mirza M, Volz C, Karlstetter M, et al. Progressive retinal degeneration and glial activation in the CLN6 (nclf) mouse model of neuronal ceroid lipofuscinosis: a beneficial effect of DHA and curcumin supplementation. *PLoS One*. 2013;8:e75963.

12. Katz ML. Potential role of retinal pigment epithelial lipofuscin accumulation in age-related macular degeneration. *Arch Gerontol Geriatr*. 2002;34:359–370.

13. Koenekoop RK. The gene for Stargardt disease, ABCA4 is a major retinal gene: a mini-review. *Ophthalmic Genetics*. 2003;24:75.

14. Menzies FM, Fleming A, Rubinsztein DC. Compromised autophagy and neurodegenerative diseases. *Nat Rev Neurosci*. 2015;16:345–357.

15. Mitter SK, Song C, Qi X, et al. Dysregulated autophagy in the RPE is associated with increased susceptibility to oxidative stress and AMD. *Autophagy*. 2014;10:1989–2005.

16. Wavre-Shapton ST, Calvi AA, Turmaine M, et al. Photoreceptor phagosome processing defects and disturbed autophagy in retinal pigment epithelium of Cln3Deltaex1-6 mice modelling juvenile neuronal ceroid lipofuscinosis (Batten disease). *Hum Mol Genet*. 2015;24:7060–7074.

17. Leinonen H, Keksa-Goldsteine V, Ragauskas S, et al. Retinal degeneration in a mouse model of CLN5 disease is associated with compromised autophagy. *Sci Rep*. 2017;7:1597.

18. Chinchore Y, Mitra A, Dolph PJ. Accumulation of rhodopsin in late endosomes triggers photoreceptor cell degeneration. *PLoS Genet*. 2009;5:e1000377.

19. Bronson RT, Donahue LR, Johnson KR, Tanner A, Lane PW, Faust JR. Neuronal ceroid lipofuscinosis (nclf), a new disorder of the mouse linked to chromosome 9. *Am J Med Genet*. 1998;77:289–297.

20. Vessey KA, Greferath U, Jobling AI, et al. Ccl2/Cx3cr1 knockout mice have inner retinal dysfunction but are not an accelerated model of AMD. *Invest Ophthalmol Vis Sci*. 2012;53:7833–7846.

21. Vessey KA, Waugh M, Jobling AI, et al. Assessment of retinal function and morphology in aging Ccl2 knockout mice. *Invest Ophthalmol Vis Sci*. 2015;56:1238–1252.

22. Vessey KA, Wilkinson-Berka JL, Fletcher EL. Characterization of retinal function and glial cell response in a mouse model of oxygen-induced retinopathy. *J Comp Neurol*. 2011;519:506–527.

23. Jobling AI, Vessey KA, Waugh M, Mills SA, Fletcher EL. A naturally occurring mouse model of achromatopsia: characterization of the mutation in cone transducin and subsequent retinal phenotype. *Invest Ophthalmol Vis Sci*. 2013;54:3350–3359.

24. Lyubarsky A, Nikonov S, Pugh EN Jr. The kinetics of inactivation of the rod phototransduction cascade with constant Ca2+i. *J Gen Physiol*. 1996;107:19–34.

25. Ho T, Vessey KA, Cappai R, et al. Amyloid precursor protein is required for normal function of the rod and cone pathways in the mouse retina. *PLoS One*. 2012;7:e29892.

26. Vessey KA, Gu BJ, Jobling AI, et al. Loss of function of P2X7 receptor scavenger activity in aging mice: a novel model for investigating the early pathogenesis of age-related macular degeneration. *Am J Pathol*. 2017;187:1670–1685.

27. Yao J, Jia L, Shelby SJ, et al. Circadian and noncircadian modulation of autophagy in photoreceptors and retinal pigment epithelium. *Invest Ophthalmol Vis Sci*. 2014;55: 3237–3246.

28. Zhou Z, Doggett TA, Sene A, Apte RS, Ferguson TA. Autophagy supports survival and phototransduction protein levels in rod photoreceptors. *Cell Death Differ*. 2015;22:488–498.

29. Ho T, Jobling AI, Greferath U, et al. Vesicular expression and release of ATP from dopaminergic neurons of the mouse retina and midbrain. *Front Cell Neurosci*. 2015;9:389.

30. Ouseph MM, Kleinman ME, Wang QJ. Vision loss in juvenile neuronal ceroid lipofuscinosis (CLN3 disease). *Ann N Y Acad Sci*. 2016;1371:55–67.

31. Tarkkanen A, Haltai M, Merenmies L. Ocular pathology in infantile type of neuronal ceroid-lipofuscinosis. *J Pediatr Ophthalmol*. 1977;14:235–241.

32. Charbel Issa P, Barnard AR, Singh MS, et al. Fundus autofluorescence in the Abca4(-/-) mouse model of Stargardt disease–correlation with accumulation of A2E, retinal function, and histology. *Invest Ophthalmol Vis Sci*. 2013;54:5602–5612.

33. Secondi R, Kong J, Blonska AM, Staurenghi G, Sparrow JR. Fundus autofluorescence findings in a mouse model of retinal detachment. *Invest Ophthalmol Vis Sci*. 2012;53:5190–5197.

34. Fogerty J, Besharse JC. Subretinal infiltration of monocyte derived cells and complement misregulation in mice with AMD-like pathology. *Adv Exp Med Biol*. 2014;801:355–363.

35. Wang NK, Fine HF, Chang S, et al. Cellular origin of fundus autofluorescence in patients and mice with a defective NR2E3 gene. *Br J Ophthalmol*. 2009;93:1234–1240.

36. Grey AC, Crouch RK, Koutalos Y, Schey KL, Ablonczy Z. Spatial localization of A2E in the retinal pigment epithelium. *Invest Ophthalmol Vis Sci*. 2011;52:3926–3933.

37. Sparrow JR, Parish CA, Hashimoto M, Nakanishi K. A2E, a lipofuscin fluorophore, in human retinal pigmented epithelial cells in culture. *Invest Ophthalmol Vis Sci*. 1999;40:2988–2995.

38. Seigel GM, Lotery A, Kummer A, et al. Retinal pathology and function in a Cln3 knockout mouse model of juvenile neuronal ceroid lipofuscinosis (batten disease). *Mol Cell Neurosci*. 2002;19:515–527.

39. Seigel GM, Wagner J, Wronska A, Campbell L, Ju W, Zhong N. Progression of early postnatal retinal pathology in a mouse model of neuronal ceroid lipofuscinosis. *Eye (Lond)*. 2005;19: 1306–1312.

40. Damme M, Brandenstein L, Fehr S, et al. Gene disruption of Mfsd8 in mice provides the first animal model for CLN7 disease. *Neurobiol Dis*. 2014;65:12–24.

41. Hafler BP, Klein ZA, Jimmy Zhou Z, Strittmatter SM. Progressive retinal degeneration and accumulation of autofluorescent lipopigments in Progranulin deficient mice. *Brain Res*. 2014;1588:168–174.

42. Wang L, Cano M, Handa JT. p62 provides dual cytoprotection against oxidative stress in the retinal pigment epithelium. *Biochim Biophys Acta*. 2014;1843:1248–1258.

43. Brandenstein L, Schweizer M, Sedlacik J, Fiehler J, Storch S. Lysosomal dysfunction and impaired autophagy in a novel mouse model deficient for the lysosomal membrane protein Cln7. *Hum Mol Genet*. 2016;25:777–791.

44. Palmer DN, Barry LA, Tyynela J, Cooper JD. NCL disease mechanisms. *Biochim Biophys Acta*. 2013;1832:1882–1893.

45. Ezaki J, Wolfe LS, Higuti T, Ishidoh K, Kominami E. Specific delay of degradation of mitochondrial ATP synthase subunit c in late infantile neuronal ceroid lipofuscinosis (Batten disease). *J Neurochem*. 1995;64:733–741.

46. Kominami E, Ezaki J, Muno D, Ishido K, Ueno T, Wolfe LS. Specific storage of subunit c of mitochondrial ATP synthase in lysosomes of neuronal ceroid lipofuscinosis (Batten's disease). *J Biochem*. 1992;111:278–282.

47. Palmer DN, Fearnley IM, Walker JE, et al. Mitochondrial ATP synthase subunit c storage in the ceroid-lipofuscinoses (Batten disease). *Am J Med Genet*. 1992;42:561–567.

48. Chinchore Y, Begaj T, Wu D, Drokhlyansky E, Cepko CL. Glycolytic reliance promotes anabolism in photoreceptors. *Elife*. 2017;6:e25946.

49. Giarmarco MM, Cleghorn WM, Sloat SR, Hurley JB, Brockerhoff SE. Mitochondria maintain distinct Ca(2+) pools in cone rhotoreceptors. *J Neurosci*. 2017;37:2061–2072.

50. Kageyama GH, Wong-Riley MT. The histochemical localization of cytochrome oxidase in the retina and lateral geniculate nucleus of the ferret, cat, and monkey, with particular reference to retinal mosaics and ON/OFF-center visual channels. *J Neurosci*. 1984;4:2445–2459.

51. Wong-Riley MT. Energy metabolism of the visual system. *Eye Brain*. 2010;2:99–116.

52. Perkins GA, Ellisman MH, Fox DA. Three-dimensional analysis of mouse rod and cone mitochondrial cristae architecture: bioenergetic and functional implications. *Mol Vis*. 2003;9:60–73.

53. Carter-Dawson LD, LaVail MM. Rods and cones in the mouse retina. I. Structural analysis using light and electron microscopy. *J Comp Neurol*. 1979;188:245–262.

54. Tanna P, Strauss RW, Fujinami K, Michaelides M. Stargardt disease: clinical features, molecular genetics, animal models and therapeutic options. *Br J Ophthalmol*. 2017;101:25–30.

55. Tsybovsky Y, Molday RS, Palczewski K. The ATP-binding cassette transporter ABCA4: structural and functional properties and role in retinal disease. *Adv Exp Med Biol*. 2010;703: 105–125.

56. Swaroop A, Chew EY, Rickman CB, Abecasis GR. Unraveling a multifactorial late-onset disease: from genetic susceptibility to disease mechanisms for age-related macular degeneration. *Annu Rev Genomics Hum Genet*. 2009;10:19–43.